ORIGINAL PAPER-EXPLORATION GEOPHYSICS

Gas-generative potential for the post-Messinian megasequence of Nile Delta Basin: a case study of Tao Field, North Sinai Concession, Egypt

Mohammad Abdelfattah Sarhan[1,2]

Abstract

The main aim of the article is to evaluate the gas potentiality for the post-Messinian megasequence in TAO Field, North Sinai Concession, offshore Nile Delta Basin. The detailed petrophysical analysis for three deviated wells in the study area (Tao-3 ST1 Well, Tao-5 STA Well and Tao-7 Well) revealed that the Pliocene Kafr El-Sheikh Formation includes eleven gas-bearing zones. These zones were named: A, B, C in Tao-3 ST1 Well and D, E, F in Tao-5 STA Well. In Tao-7 Well, the interesting zones are named G, H, I, J and K. All of these sandy intervals are relatively shallow in depth and differ in thickness between 4 and 56 m. These zones are characterized by shale volume (10%), total porosity (30–40%), effective porosity (30–35%), gas saturation (50–90%), high effective permeability to gas and low permeability to water. The seismic data displayed that listric faults and the associated rollover folds have an important role in forming structural traps for the examined gas-bearing zones in Tao Field and its surroundings. This work revealed that the success rate in discovering new gas prospects within the Pliocene–Pleistocene succession at North Sinai Concession is very high.

Keywords Nile Delta Basin · North Sinai Concession · Sheet sand reservoir · Post-Messinian · Tao Field

Introduction

The Nile Delta Basin is a huge gas province in the eastern Mediterranean region (Dolson et al. 2002). Recently, numerous gas discoveries, from Oligocene to Quaternary, were explored.

The Nile Delta Basin is holding about 223 trillion cubic feet of gas reserves in more than 126 fields scattered in the Nile Cone (Kirschbaum et al. 2010). These fields were principally generated from mature source rocks found in the Neogene deltaic sequence, as well as a large biogenic gas source (Vandré et al. 2007). The gas exploration in Nile Delta Basin started since the discovery of the Abu Madi Field in 1967 from clastic plays. The Abu Madi Field was followed by the Baltim discovery from the buried Miocene channels which were deposited throughout the Messinian Salinity crisis. In the 1980s, deeper targets corresponding to the Middle Miocene sandstones were discovered in El-Temsah Field.

In the 1990s, the exploration process in the Nile Delta Basin was concerned with the ultra-deeper water from the Pliocene turbidite plays (e.g. Ha'py Field). Recently, the Early Miocene-Oligocene sands also yielded good results in the Nile Delta Basin, such as Raven Field (Esestime et al. 2016). In 2015, ENI Company drilled a new play close to the Egypt/Cyprus boundary at water depth of 1500 m. This play represents a very large carbonate platform corresponding to the Early-Middle Miocene age and lies beneath a thick section of Messinian evaporates. This target was drilled by the Zohr-1 Well. The gross thickness of this discovery was found to hold a 628 m of gas column and net pay of 430 m. The gas in place was initially estimated at 30 TCF (Esestime et al. 2016).

The sands of the Early-Middle Pliocene (Kafr El-Sheikh Formation) in addition to the Late Pliocene (El-Wastani Formation) characterize the most optimistic targets for gas exploration within the offshore portions of the Nile Delta (e.g. Lashin and Mogren 2012; Othman, et al. 2018; Abd El-Gawad et al. 2019; Leila and Mohamed 2020; Elatrash et al. 2021). This is because the Pliocene sequence in Nile

✉ Mohammad Abdelfattah Sarhan
  msarhan@du.edu.eg

1 Geology Department, Faculty of Science, Damietta University, New Damietta City 34517, Egypt

2 Center of Space Research and Applications (CSRA), Damietta University, New Damietta City, Egypt

Delta Basin does not include challenges in exploring new plays. These hardships exist in the pre-Messinian sequence, including the high pressure, the poor seismic imaging and the absence of direct hydrocarbon indicators (Dolson et al. 2002). Many of the discovered gas in Nile Delta Basin are biogenic (mainly methane) in origin. Also, a thermogenic source lies beneath the Nile Delta which has been proved by minor oil discovery particularly in the Pre-Pliocene discoveries (Esestime et al. 2016).

The Pliocene clastics in the Nile Delta Basin display an outboard progradation with time and are one of the chief hydrocarbons plays. The Pliocene sandy intervals are usually unconsolidated and have excellent reservoir properties with porosity varying between 24 and 36% and the net sand is expected to be 30–90% (Abdel Aal et al. 2000). The Pliocene sediments contain turbidites at the slope and basin floor in the form of channel, channel levees and sheet sands (Abdel Aal et al. 2000). The principle axis of Pliocene deposition trends SE-NW over the existence of rotated fault block. Several buried channels are cut by large salt-induced faults providing attractive exploration targets (Abdel Aal et al. 2000). The Pliocene channel plays have been demonstrated by successful explored wells at offshore Nile Delta Basin, such as Seth, Ha'py, Seti, Osiris, Rosetta, Saffron and Scarab discoveries (Abdel Aal et al. 2000). The Pliocene slope-turbidite plays (such as Sapphire, Sienna, Simian and Taurus) represent recent discoveries in the western offshore parts of Nile Delta Basin (Abdel Aziz and Shann 2005).

The North Sinai Concession is situated within the eastern flank of Nile Delta cone in the Mediterranean Sea, about 65 km northeast of Port Said City. It involves three separate fields: Tao, Kamose and Seti-Plio with whole area of about 383 Km^2 (Ewida, and Darwesh 2010) as shown in Fig. 1. The present study concerns with Tao Field which covers an area of about 143 km^2 between latitudes: 31.5–32° N and longitudes 32.5–33° E in North Sinai Concession (Fig. 1).

The offshore portion of Sinai conserves good conditions for hydrocarbon accumulation and needs more intensive exploration (Abd-Allah et al. 2020). Also, the Pliocene–Pleistocene section in TAO Field is still promising for hosting shallow gas reservoirs located close to numerous hydrocarbon discoveries which merits further exploration by NOSPCO (Ewida and Darwesh 2010). Consequently, the current work aims to assess the gas potentiality of the Post-Messinian sandy intervals in Tao Field. This goal has been achieved through evaluating the petrophysical parameters for the sand-intervals in three deviated wells in Tao Field (Tao-3 ST1, Tao-5 STA and Tao-7 wells). This aids in assessing the quality of the gas reservoir and adds new economic reserves to natural gas resources existing at North Sinai Concession, offshore Nile Delta Basin.
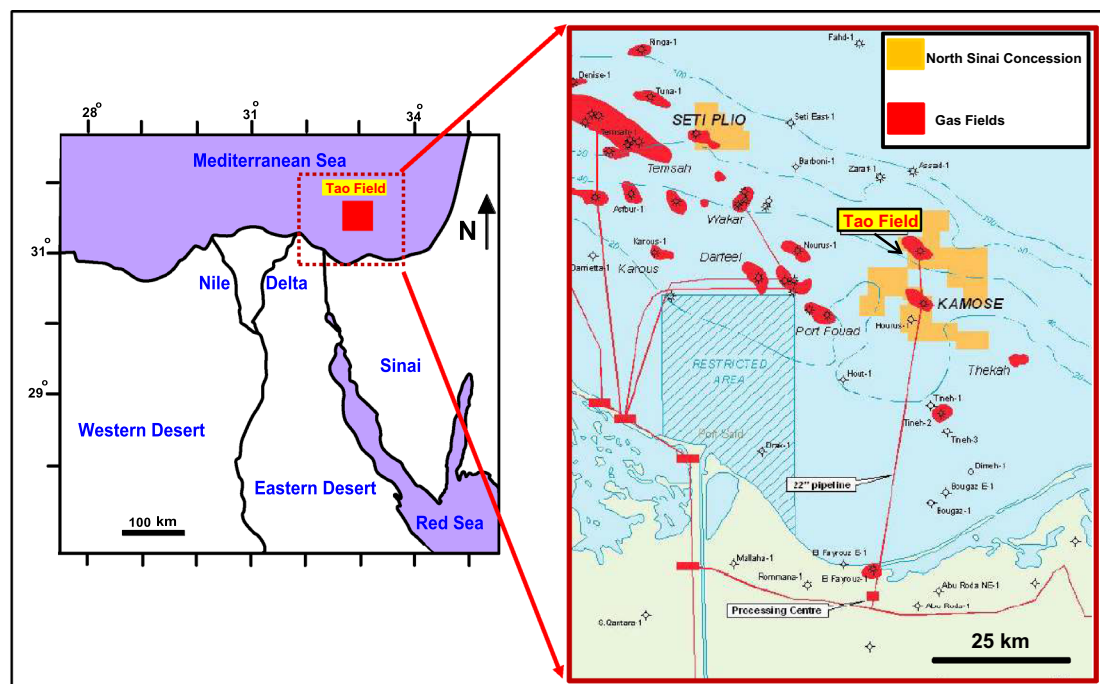

Fig. 1 Map shows the location of Tao Field at North Sinai Concession, offshore Nile Delta Basin

Geologic setting

The Nile Delta Basin is located at the eastern Mediterranean province covering an area of approximately 250,000 km² (Kirschbaum et al. 2010). It was originated as a passive margin basin in Late Triassic—Early Cretaceous times due to the thermal subsidence followed the rifting phase which was characterized by NW–SE and E–W trending basins (May 1991; Dolson et al. 2001; Loutit et al. 2001). The hinge line in the Nile Delta Basin is an E–W oriented fault representing the southern boundary of the thick Neogene section to the north of the Nile Delta provenance (Harms and Wray 1990).

During the Senonian-Eocene times, these basins were inverted producing series of NE–SW oriented folds of the Syrian arc system (Moustafa and Khalil 1995; Abd-Allah 2008). Throughout the Late Miocene times, a subsequent extensional tectonic phase with dominant NW oriented faults affected the Nile Delta Basin resulting from the NNW propagation of the Gulf of Suez rifting phase (Sarhan et al. 2014).

Throughout the Messinian time (7.24–5.33 Ma), the Mediterranean Sea was isolated from the Atlantic Ocean. Consequently, this was followed by an eustatic sea level falling which developed large system of paleo-canyons incised the area around the Mediterranean region (Barber 1981; Sestini 1989; Harms and Wary 1990; Dolson et al. 2002; Salem et al. 2005). This sea level falling stage was tracked by major marine flooding phase during the Pliocene age (5.3 m y) (Lourens et al. 1996) due to the re-reconnection between the Mediterranean Sea and the Atlantic Ocean (Ruggieri and Sprovieri 1976).

The Pliocene–Quaternary section in the Nile Delta Basin is a post-rift megasequence (Sarhan et al. 2014) and is usually referred to as post-Messinian megasequence (e.g. Sarhan and Safa 2019). This megasequence was deposited under an active prograding phase associated with the influence of clastics charge from distal fluvial system located to the south (El-Fawal et al. 2016).

The stratigraphy of Post-Messinian megasequence in Nile Delta Basin encompasses Kafr El Sheikh Formation of Early–Middle Pliocene, El Wastani Formation and Mit Ghamr Formation of Late Pliocene, Bilqas Formation of Quaternary age (EGPC 1994), as shown in Fig. 2. Kafr El-Sheikh Formation was deposited in an outer shelf marine setting, while El Wastani Formation characterizes the delta front sub-environment, but Mit Ghamr Formation displays the distributary mouth bars of the deltaic sequence (El-Fawal et al. 2016).

The sandy intervals of Kafr El-Sheikh Formation signify the principal gas reservoirs for numerous new discoveries in Nile Delta Basin with thick net pays (Mohamed 2004).

Data and methodology

The accessible geophysical data in the present study encompasses twenty-two 2D seismic sections covering the study area (Fig. 3). The seismic data has been tied to three deviated wells (Tao-3 ST1, Tao-5 STA and Tao-7) drilled in Tao Field at North Sinai Concession using Petrel Software of Schlumberger (Figs. 4, 5 and 6). The available wireline logs data for these wells include as follows: Calliper, Corrected Density, Gamma Ray, Sonic, Resistivity, Neutron and Density logs. The mud log for Tao-3 ST1 Well in addition to the composite logs for Tao-5 STA and Tao-7 wells are also available encompassing the lithologic description and the chromatograph analysis which is helpful in referring to the hydrocarbons bearing zones.

The objective of the present work has been performed through the qualitative examination for the available mud and composite logs of the examined wells to discriminate the possible hydrocarbon-bearing zones within the Pliocene–Pleistocene section. This step has revealed eleven sandstones intervals displaying positive signs for being gas-holding zones. These zones are named A, B, C in Tao-3 ST1 Well and D, E, F in Tao-5 STA Well. However, in Tao-7 Well, the interesting zones are named G, H, I, J and K. The optimistic signs opposite these zones encompass the high values of the chromatograph analysis, especially for methane, Ethan and butane content (supporting the presence of gas rather than oil). The depth interval and thickness for each zone in the investigated wells are summarized in Table 1.

The suites of the wireline logs represent the interesting zones that have been quantitatively appraised using Techlog Software of Schlumberger. This evaluation encompasses the calculations of the primary petrophysical parameters which are important for describing the potentiality for hydrocarbon reservoirs. These parameters include as follows: shale volume (Vsh), total porosity (ϕ_T), effective porosity (ϕ_e), water saturation (S_w) and bulk volume of water (BVW).

Shale volume (Vsh)

Shale volume displays the amount of clay in the examined zones. It can be calculated from different wireline logs, such as gamma ray, neutron and density logs. Vsh is expressed as a percentage or fraction. It has been determined in this work from gamma ray log as a linear response and displayed in track four of figure B in Figs. 7, 8, 9, 10, 11, 12, 13, 14, 15, 16 and 17 using the following relationship after Fertl and Frost (1980):-

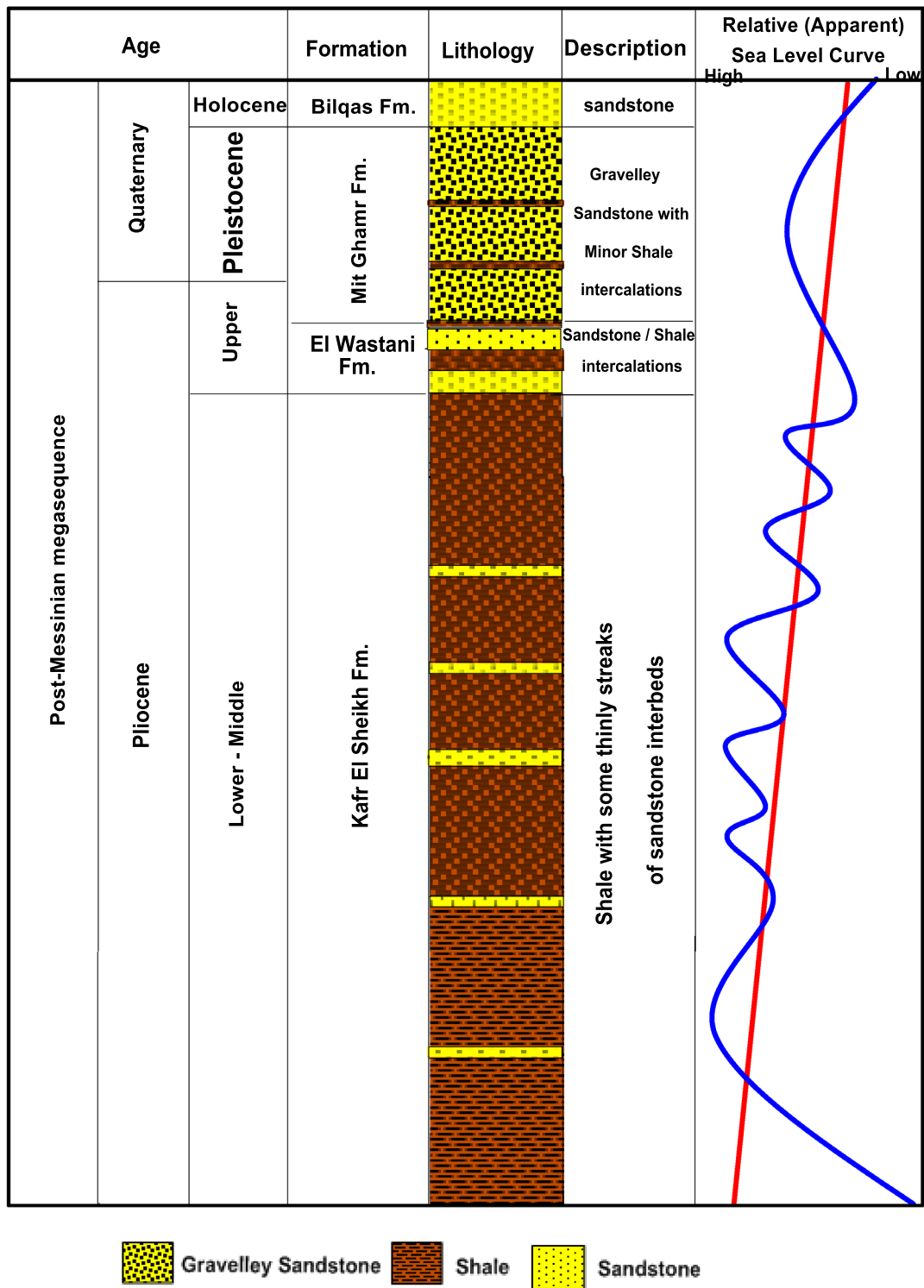$$V_{sh} = \frac{(GR - GR_{min})}{(GR_{max} - GR_{min})} \tag{1}$$

Fig. 2 Lithostratigraphic column at Tao Field, North Sinai Concession, offshore Nile Delta Basin. Note that the red line displays the long-term eustatic curve after Haq et al, (1987) and the blue line represents the relative sea level curve after El-Fawal et al. (2016)
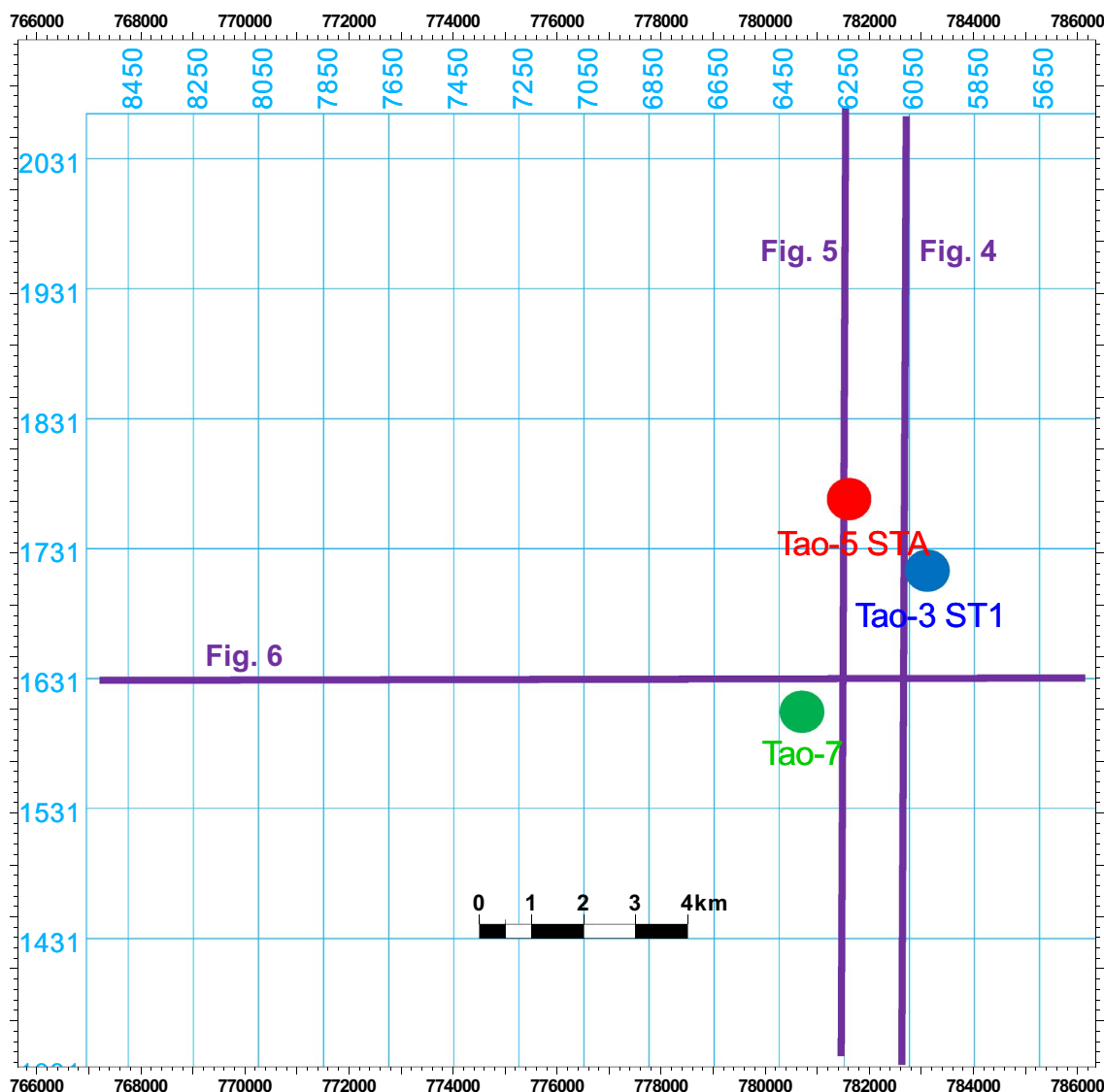
Fig. 3 Study area with accessible seismic profiles and wells locations

where **Vsh** = Shale volume; **GR** = gamma ray reading value; **GR**_{min} = lowest gamma ray value; **GR**_{max} = highest gamma ray value.

where Vsh = Shale volume; GR = gamma ray reading value; GR_{min} = lowest gamma ray value; GR_{max} = highest gamma ray value.

Total porosity (ϕ_T)

Total porosity represents the total volume of the entire void spaces within a rock and is expressed as percentage or fraction. It sums two components: primary and secondary porosities. The following formula of Asquith and Gibson (1982) has been used to calculate the total porosity based on the neutron-density porosity logs and shown in track five of figure B in Figs. 7, 8, 9, 10, 11, 12, 13, 14, 15, 16 and 17:

$$\varnothing_T = \frac{\varnothing_N + \varnothing_D}{2} \qquad (2)$$

where ϕ_T = Total porosity; ϕ_N = neutron porosity; ϕ_D = density porosity.

Effective porosity (ϕ_e)

The percent of interconnected voids in a given volume of rock which able to transmit fluids is called effective porosity (Asquith and Gibson 1982). It has been calculated by the following equation and displayed in track six of figure B in Figs. 7, 8, 9, 10, 11, 12, 13, 14, 15, 16 and 17:
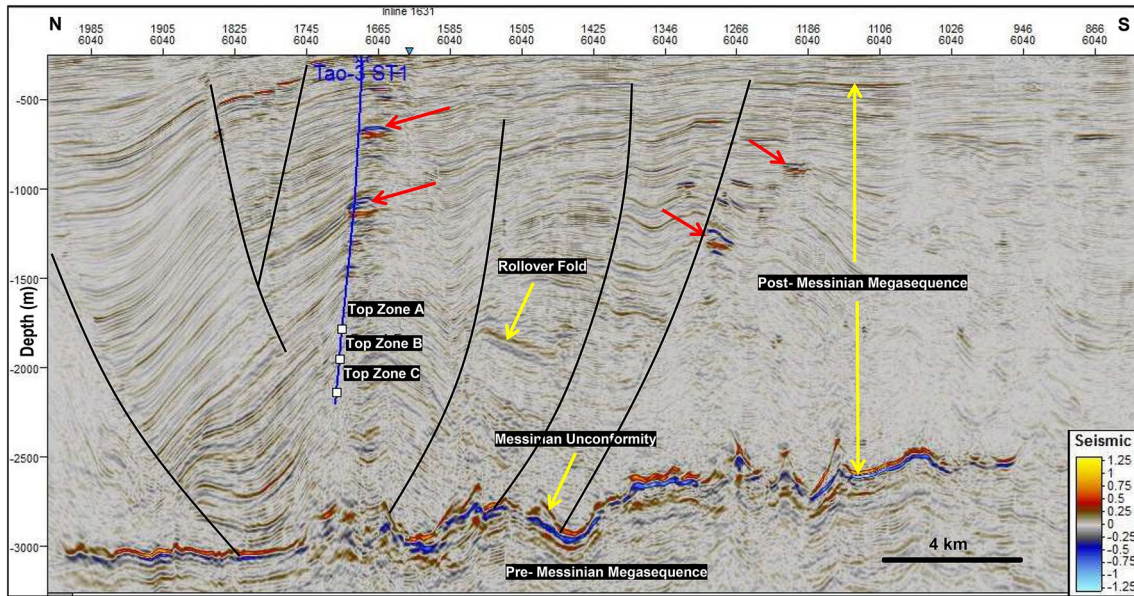
Fig. 4 North–South seismic crossline No. 6050 displays the post-Messinian megasequence in the study area and the gas-bearing zones within Tao-3 ST1 Well (zones: A, B and C). The red arrows refer to suggested bright spots which expected to be further gas-bearing zones in the study area within the post-Messinian megasequence at North Sinai Concession
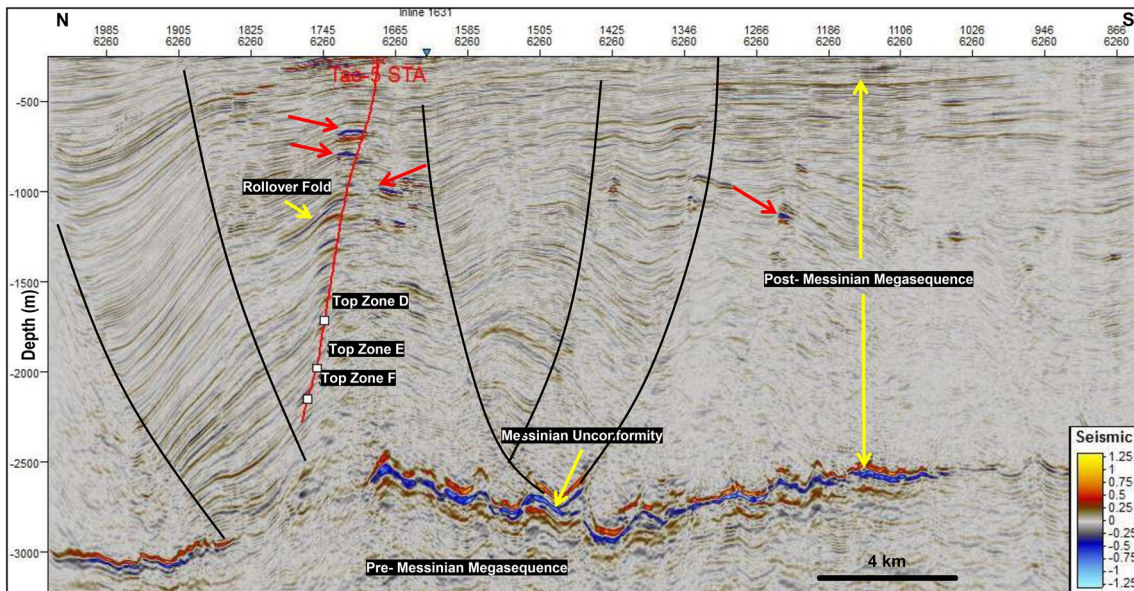

Fig. 5 North–South seismic crossline No. 6250 exhibits the gas-holding zones within Tao-5 STA Well (zones: D, E and F). The red arrows refer to suggested bright spots which expected to be further gas-bearing zones in the study area within the post-Messinian megasequence at North Sinai Concession

$$\varnothing_e = \varnothing * \left(1 - V_{sh}\right) \qquad (3)$$

where ϕ_e = Effective porosity; ϕ_T = Total porosity; V_{sh} = Shale volume.

Water saturation (S_w)

Water saturation has been computed for the inspected zones using Indonesia model of Poupon and Leveaux (1971) as
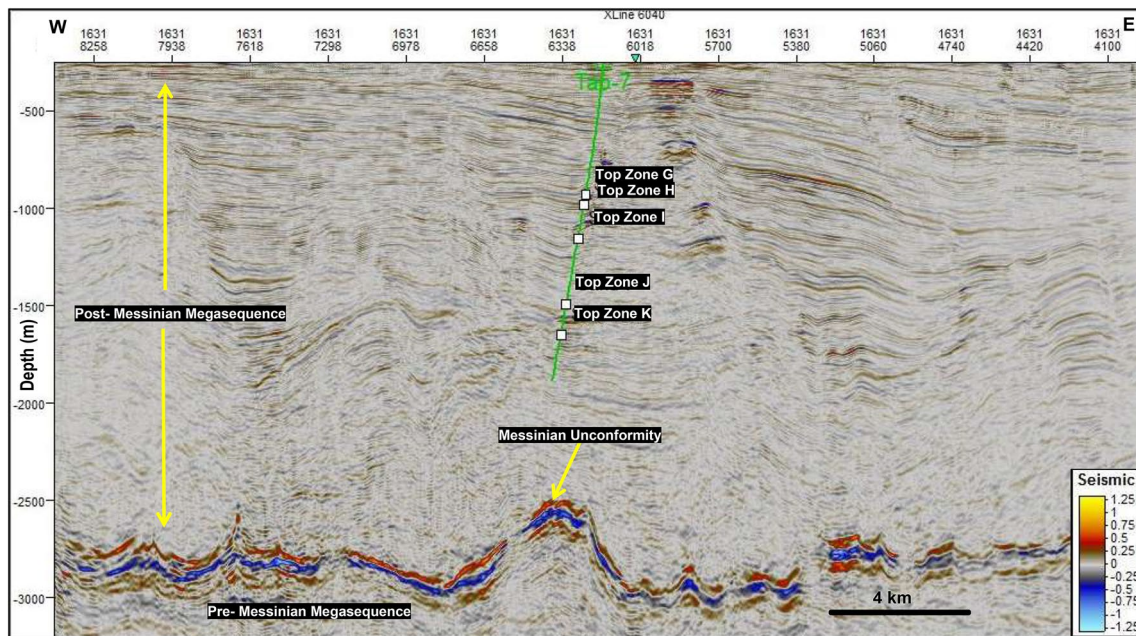
Fig. 6 East–West seismic inline No. 1631 displays the promising zones of Tao-7 Well (zones: G, H, I, J and K)

Table 1 Summary table for the promising gas-bearing zones within the examined wells at Tao Field, North Sinai Concession, offshore Nile Delta Basin, Egypt

Well name	Well location	Zone (Gas-Pay)	Measured depth "m"			True vertical depth "m"		
			From	To	Thickness	From	To	Thickness
TAO-3 ST1	31 36′ 38.51″ N 32 45′ 35.48″ E	Zone A	2235	2298	63	1821	1871	50
		Zone B	2444	2515	71	1988	2044	56
		Zone C	2628	2650	22	2133	2150	17
		Total thickness			156	Total thickness		123
TAO-5 ST A	31° 36′ 38.247″ N 32° 45′ 36.181″ E	Zone D	2500	2555	55	1751	1794	43
		Zone E	2850	2882	32	2015	2034	19
		Zone F	3169	3215	46	2197	2224	27
		Total thickness			133	Total thickness		89
TAO-7	31° 36′ 38.0915″ N 32° 45′ 36.1958″ E	Zone G	1162	1169	7	971	975	4
		Zone H	1242	1266	24	1025	1041	16
		Zone I	1509	1538	29	1201	1219	18
		Zone J	2027	2046	19	1535	1547	12
		Zone K	2270	2288	18	1691	1703	12
		Total thickness			97	Total thickness		62

follows:

$$S_w = \left\{ \left[\left(\frac{V_{sh}^{2-V_{sh}}}{R_{sh}} \right)^{1/2} + \left(\frac{\phi_e^m}{R_w} \right)^{1/2} \right]^2 R_t \right\}^{-1/n} . \quad (4)$$

where S_w = water saturation; V_{sh} = shale volume; ϕ_e = effective porosity; R_{sh} = shale resistivity; R_t = deep resistivity; R_w = connate water resistivity (set equals 0.086 $\Omega m^2/m$); m = cementation exponent (set equal 2); n = saturation exponent (set equal 2); a = tortuosity factor (set equal 1). The values of all these variables have been set according to an internal report from North Sinai Petroleum Company.
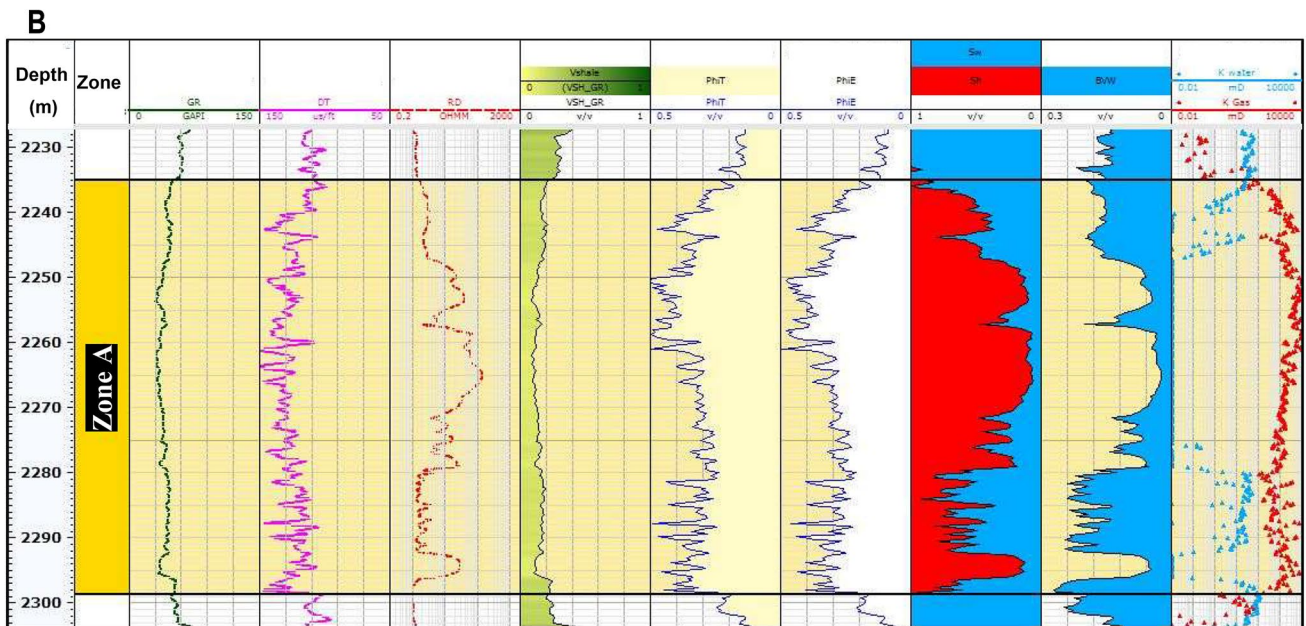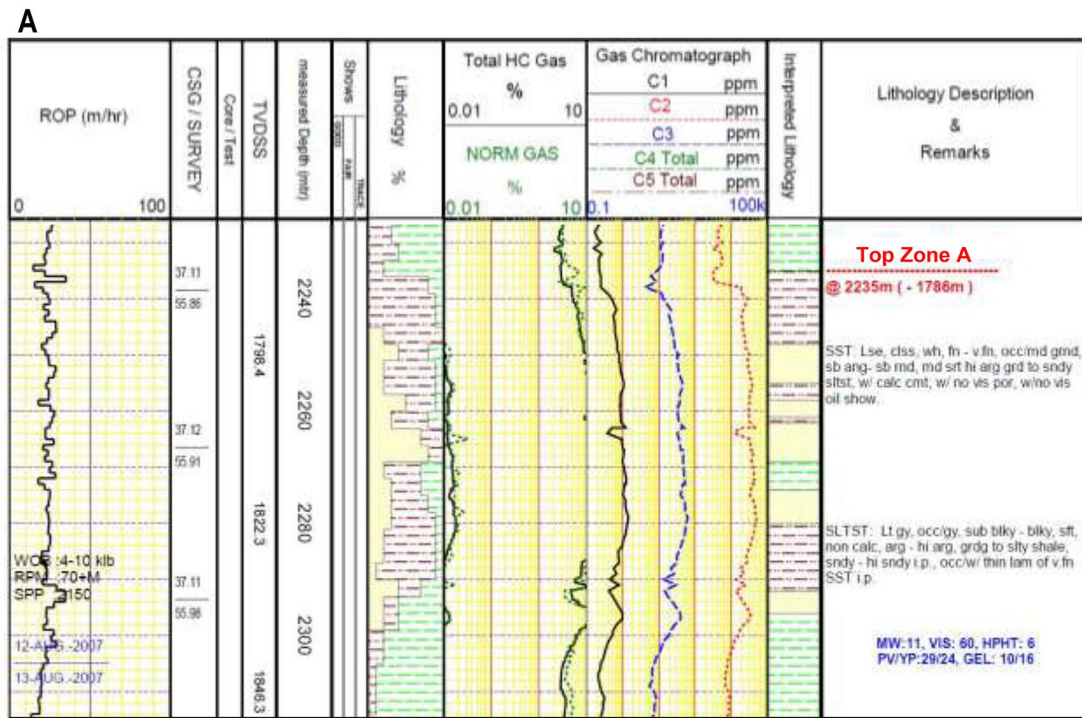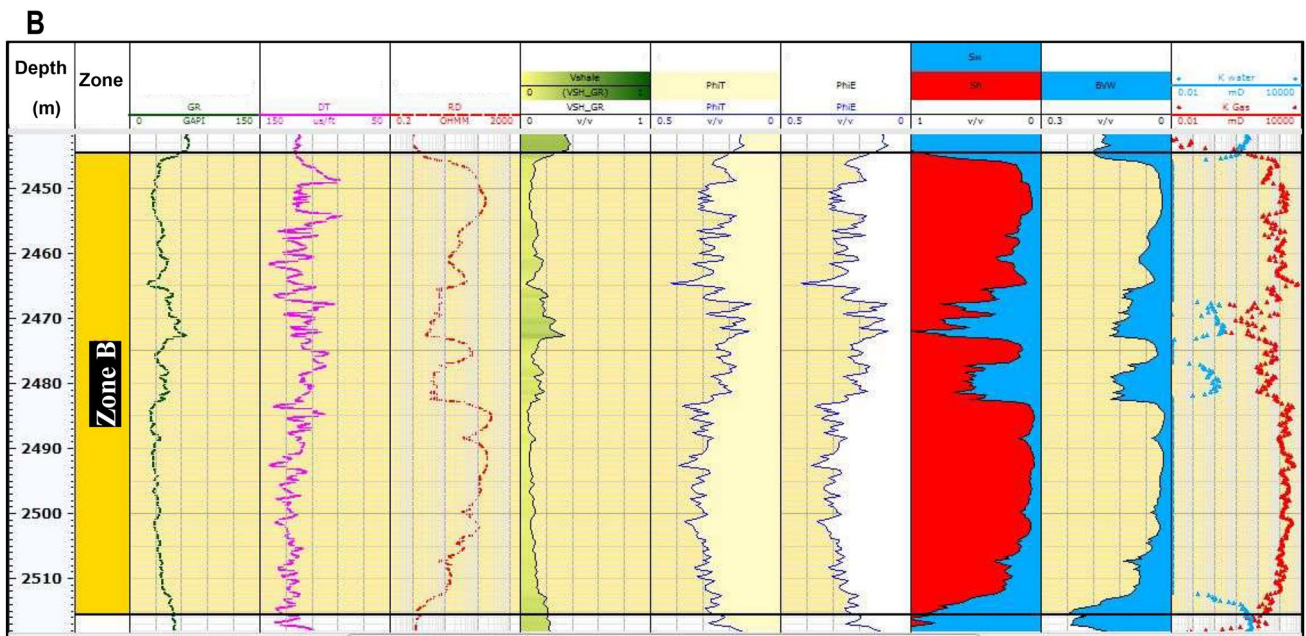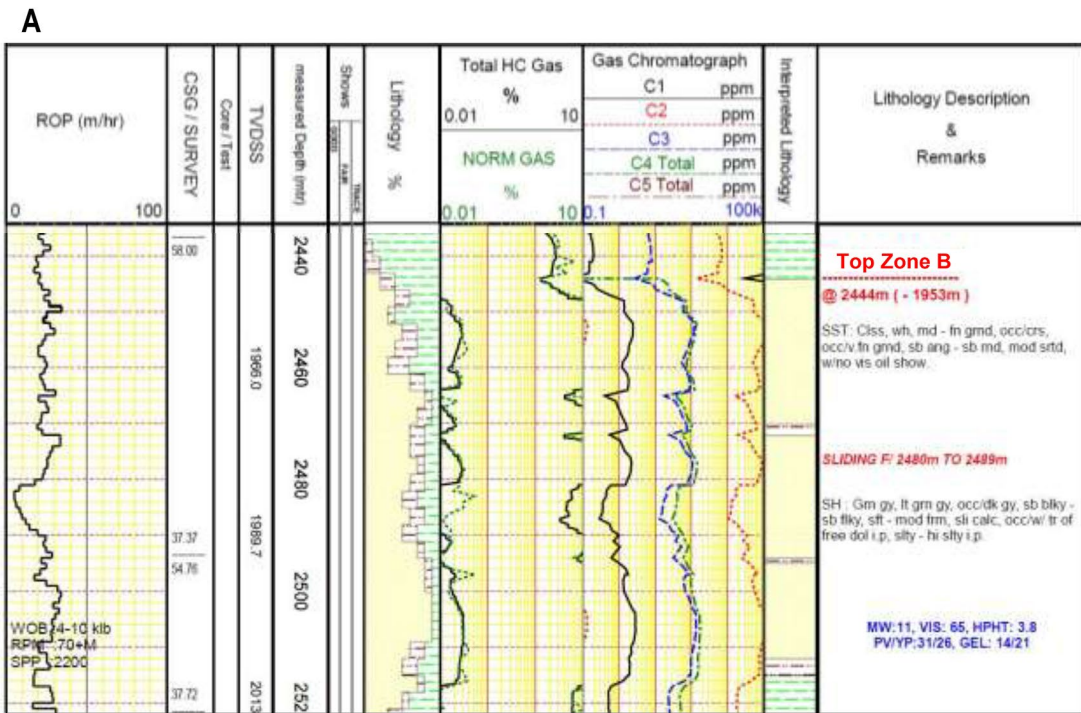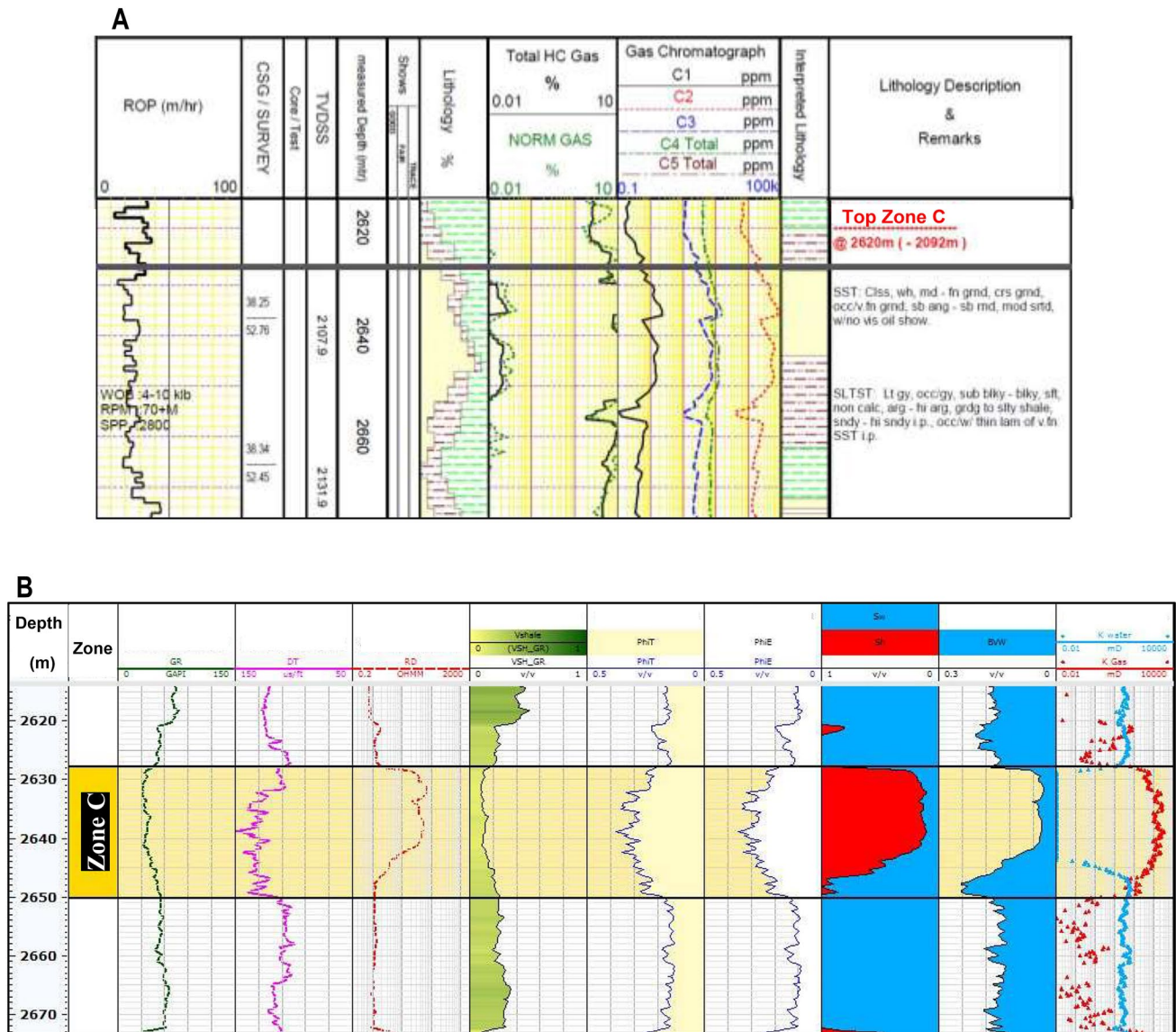
Fig. 7 **A** Mud log shows the high values of the chromatograph analysis opposite zone A within Tao-3 ST1 Well between measured depths 2235 and 2298 m. **B** Petrophysical data with interpretation for zone A represents the highly promising characteristics for gas production for zone A

The calculated water saturation values have been displayed in track seven of figure B in Figs. 7, 8, 9, 10, 11, 12, 13, 14, 15, 16 and 17 are shaded with blue colour, while the red colour in the same track refers to the gas saturation value.

Bulk volume of water (BVW)

Bulk Volume Water represents the value of water saturation times porosity. If the calculated BVW values in a specific zone are low and constant, this zone is expected to produce

Fig. 8 **A** Mud log shows the high values of the chromatograph analysis opposite zone B within Tao-3 ST1 Well between measured depths 2444 and 2515 m. **B** Petrophysical data with interpretation for zone B represents the highly promising characteristics for gas production for zone B

water-free hydrocarbon. It can be determined by applying the following equation (after Buckles 1965):

$$BVW = \phi_{e*}S_w \tag{5}$$

where ϕ_e = Effective porosity; S_w = water saturation.

The calculated BVW values have been presented in track eight of figure B in Figs. 7, 8, 9, 10, 11, 12, 13, 14, 15, 16 and 17 and are shaded with blue colour.

Fig. 9 **A** Mud log shows the high values of the chromatograph analysis opposite zone C within Tao-3 ST1 Well between measured depths 2628 and 2650 m. **B** Petrophysical data with interpretation for zone C represents the highly promising characteristics for gas production for zone C

Effective permeability

Effective gas and water permeability reflect the expected fluid flow through the production process from hydrocarbon reservoirs. The increase in values of gas permeability means the reduction in water permeability to flow out from the reservoir (accordingly, the extracted fluid during production will be gas) and vice versa.

The calculated gas permeability values have been presented in track nine (the last track) in figure B of Figs. 7, 8, 9, 10, 11, 12, 13, 14, 15, 16 and 17 and are shaded with red colour. However, the calculated water permeability values have been presented in the same track but with blue colour.

Pickett plot

Pickett plot represents the relation between deep resistivity (on the *x*-axis) and the effective porosity (on the *y*-axis) using logarithmic scales (Pickett 1972). This plot has been created to graphically display the efficiency for the interpreted zones to be promising gas-bearing intervals in the examined wells. In Tao-3 ST1 Well, the interesting zones (A, B, C) are shown in Fig. 18, while the motivating zones in Tao-5 STA Well (zones: D, E, F) are presented in Fig. 19 and the promising zones of Tao-7 Well (zones: G, H, I, J and K) are displayed in Fig. 20.
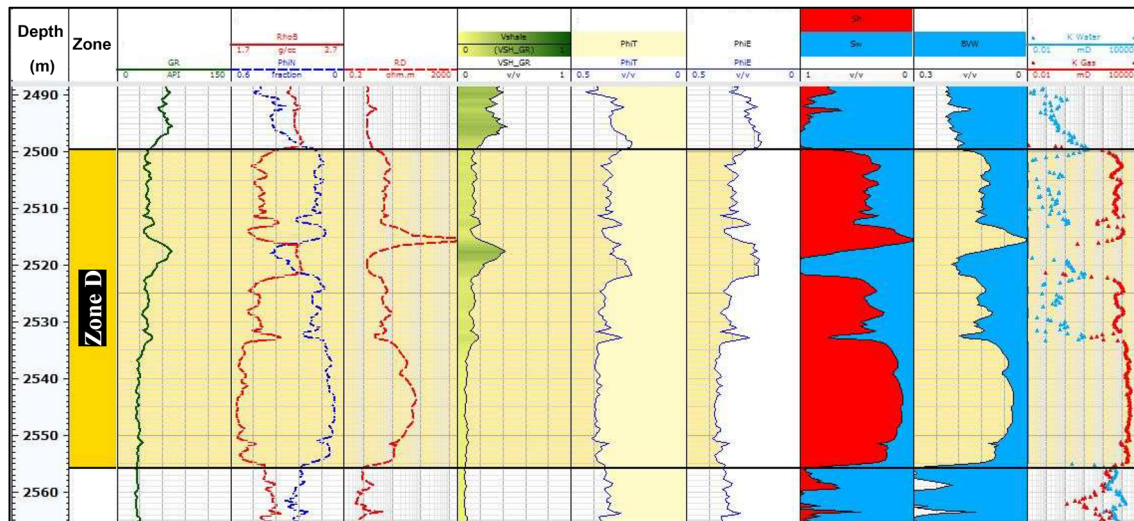
Fig. 10 Petrophysical data with interpretation for zone D between measured depths 2500 and 2555 m within Tao-5 STA Well represents the highly promising characteristics for gas production for zone D

Results and discussion

Based on the mud and composite logs for the examined wells, the entire sands of the different gas-bearing zones (A, B, C, D, E, F, G, H, I, J and K) within Kafr El-Sheikh Formation are almost similar in description. These sands are loose, colourless, white, grey, medium to fine-grained and occasionally coarse, sub-rounded to sub-angular, moderately sorted, occasionally glauconitic and with no oil shows.

The well log patterns opposite all the examined zones (A, B, C, D, E, F, G, H, I, J and K) exhibit the following nine characteristics:

1. Presence of minor shale volume evidenced by the low gamma-ray values (gamma-ray curve deflects to the left) as shown in the first track of figure B in Figs. 7, 8, 9, 10, 11, 12, 13, 14, 15, 16 and 17.
2. The neutron curve (dashed-blue curve) deflects to the right and reads low porosity due to the low interactions between neutron and hydrogen in gas zones compared to the neutron and hydrogen interactions in water zones. The density curve (solid red curve) deflects to the left due to the presence of gas minimizing the reading of density. Also, the wide separation between neutron and density curves reflects the existence of gas. Moreover, the cross-over feature between neutron and density curves confirms the sandstone matrix (second track of figure B in Figs. 10, 11, 12, 13, 14, 15, 16 and 17.
3. The deep resistivity curve deflects to the right confirming the presence of the non-conductive gas as presented in the third track of figure B in Figs. 7, 8, 9, 10, 11, 12, 13, 14, 15 and 17.

4. The calculated volume of shale in the examined zones is relatively very low (around 10%) as seen in the fourth track of figure B in Figs 7, 8, 9, 10, 11, 12, 13, 14, 15, 16 and 17.
5. The calculated total porosity in the examined zones is relatively very high (30–40%) as revealed in the fifth track of figure B in Figs 7, 8, 9, 10, 11, 12, 13, 14, 15, 16 and 17.
6. The calculated effective porosity in the inspected zones is relatively very high (30–35%) as shown in the sixth track of figure B in Figs 7, 8, 9, 10, 11, 12, 13, 14, 15, 16 and 17.
7. Most of the investigated water saturation values for the examined zones vary between 10 and 50% (i.e. gas saturation ranges between 90 and 50%) reflecting the high gas potentiality of these zones as noticed in the seventh track of figure B in Figs 7, 8, 9, 10, 11, 12, 13, 14, 15, 16 and 17.
8. The values derived for bulk volume water are relatively low as revealed in the eighth track of figure B in Figs 7, 8, 9, 10, 11, 12, 13, 14, 15, 16 and 17.
9. The increase in values of effective gas permeability and the decrease in water permeability reflect that the gas will be the expected fluid which will flow out from these zones as displayed in the last track of figure B in Figs 7, 8, 9, 10, 11, 12, 13, 14, 15, 16 and 17.

Consequently, the examination of the well logging data revealed that all the inspected zones in the examined three wells have the ultimate optimistic criteria for being gas-producer zones. The values derived for both water saturation (*Sw*) and bulk volume water (BVW) are low indicating that the examined intervals are reservoirs with a high gas
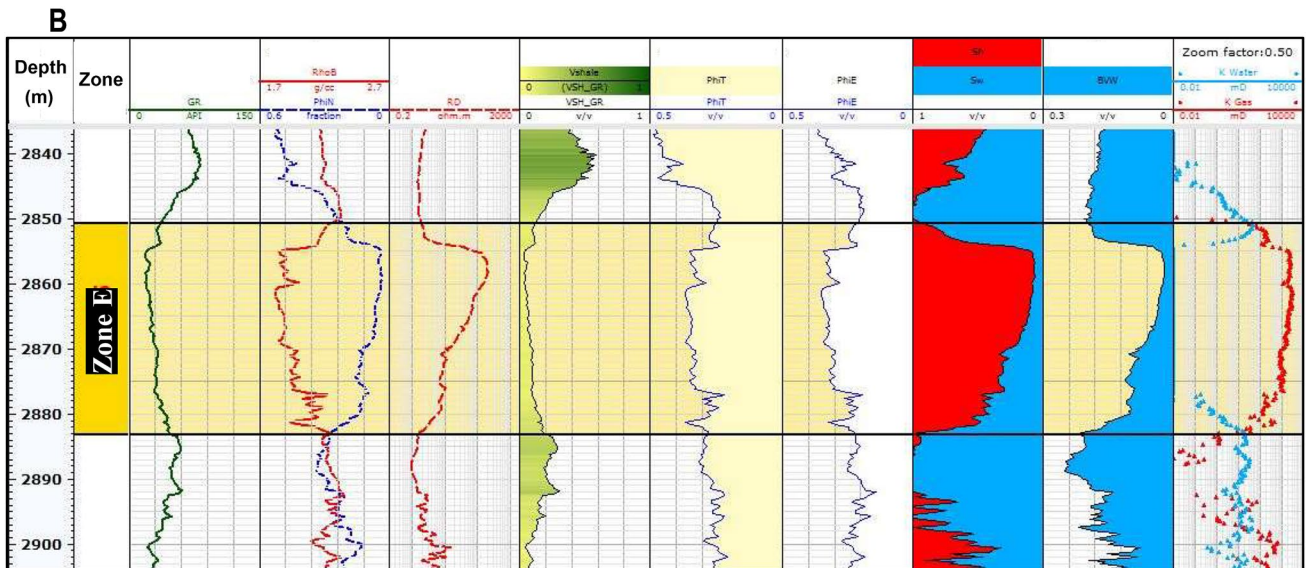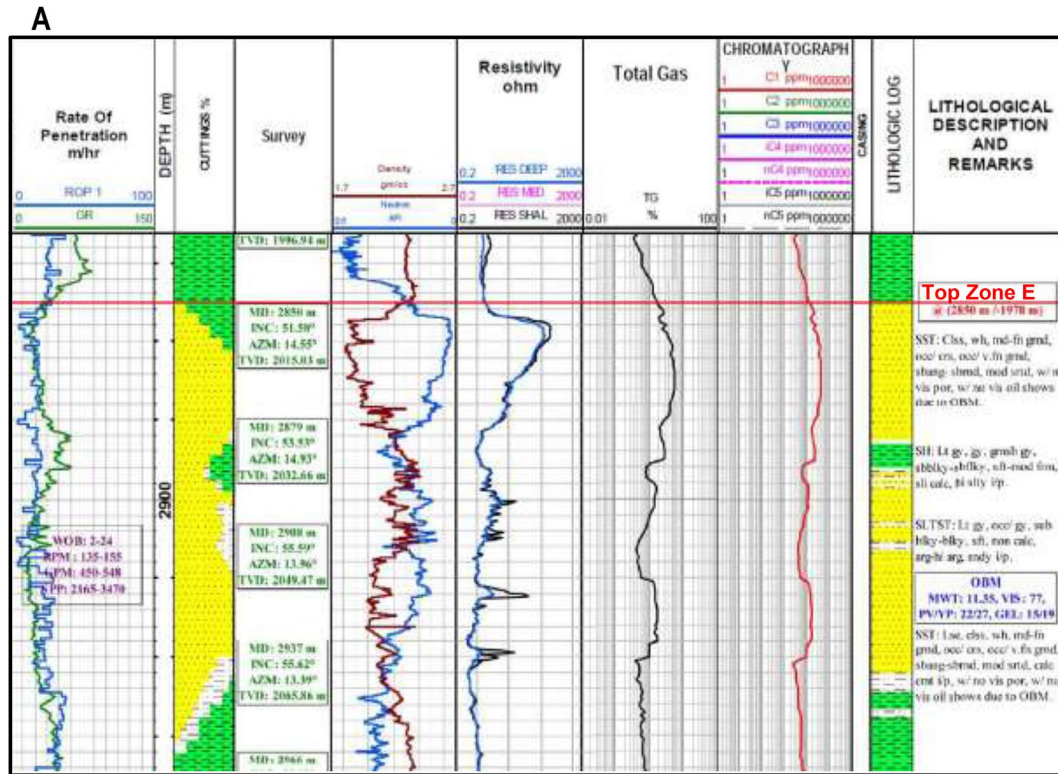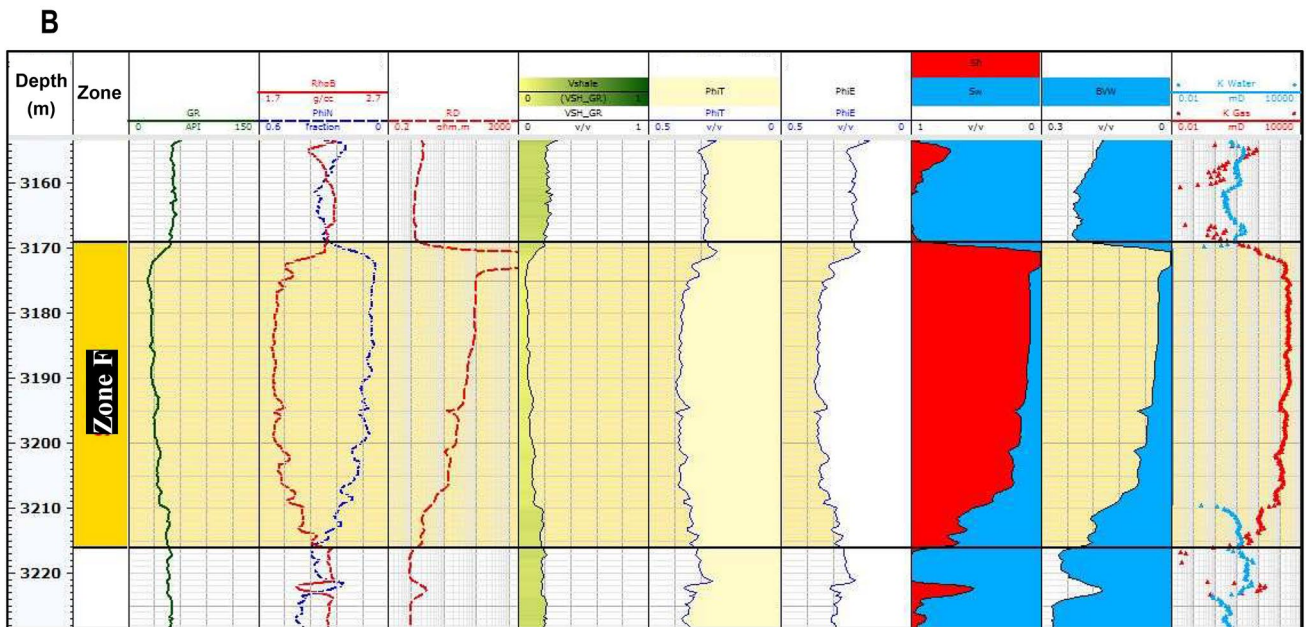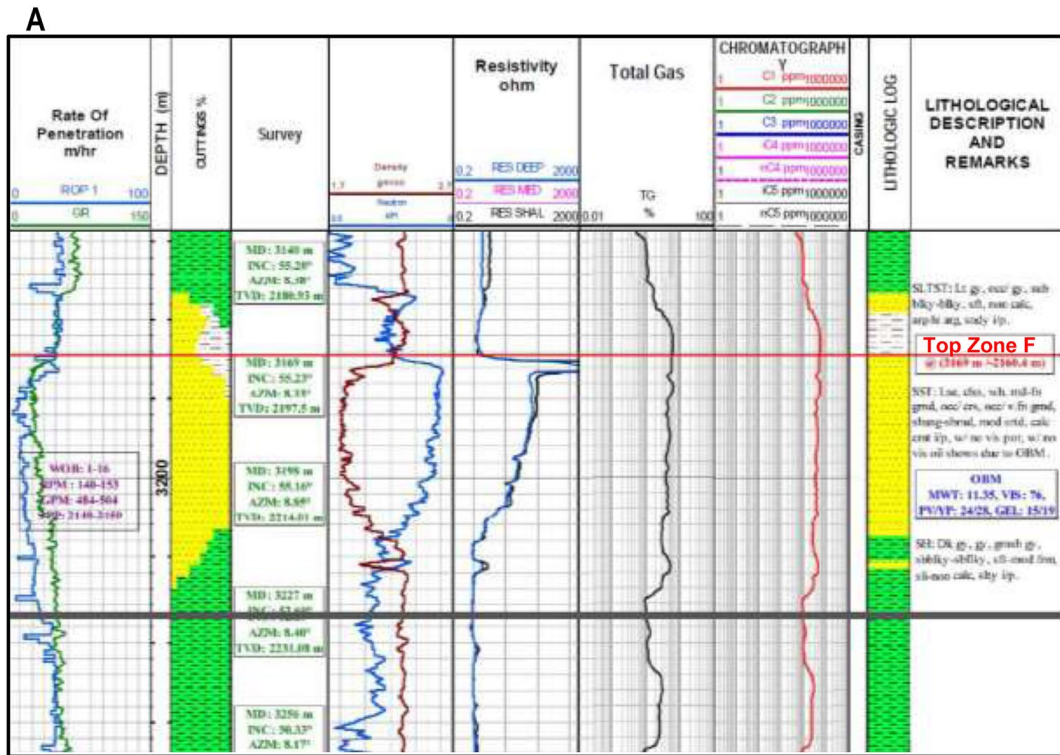
Fig. 11 A Composite log shows the high values of the chromatograph analysis and the high deep resistivity values opposite zone E within Tao-5 STA Well between measured depths 2850 and 2882 m. **B**
Petrophysical data with interpretation for zone E represents the highly promising characteristics for gas production for zone E

saturation at irreducible water saturation (Asquith and Gibson 1982).

Bright spots are the most popular features of DHI (Direct Hydrocarbon Indicators) which give indication for the occurrence of hydrocarbon on seismic sections and decrease the

risk of penetrating a dry exploration well (Hammond 1974). The bright spots are caused by the changes in seismic wave amplitude which depends on the physical properties of rocks and the included pore fluids (Gardner et al. 1974). The shallow Pliocene gas pays in Nile Delta Basin are characterized
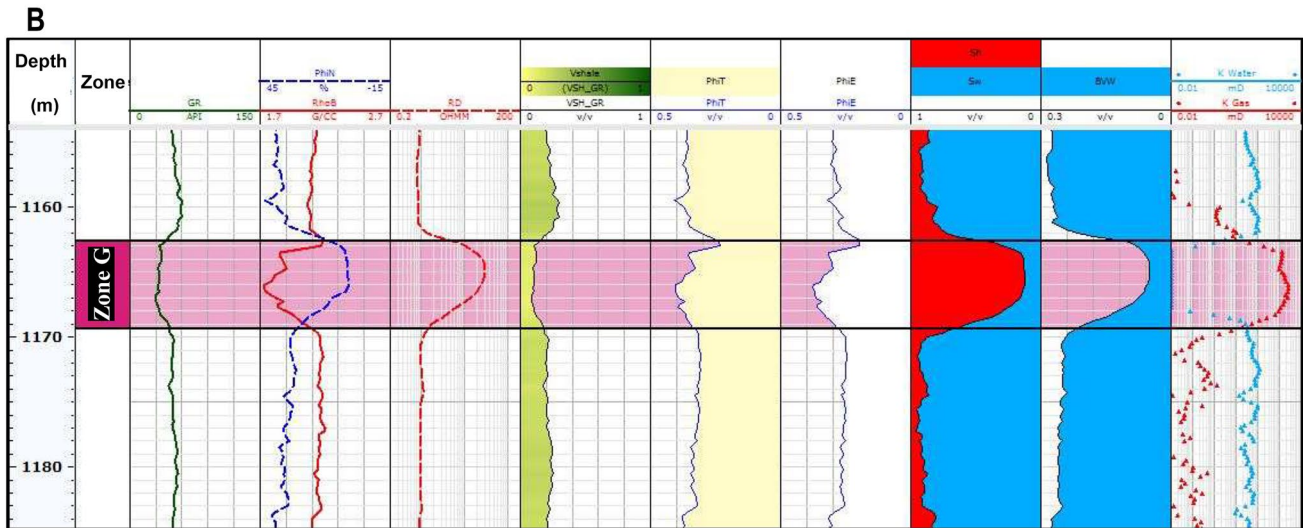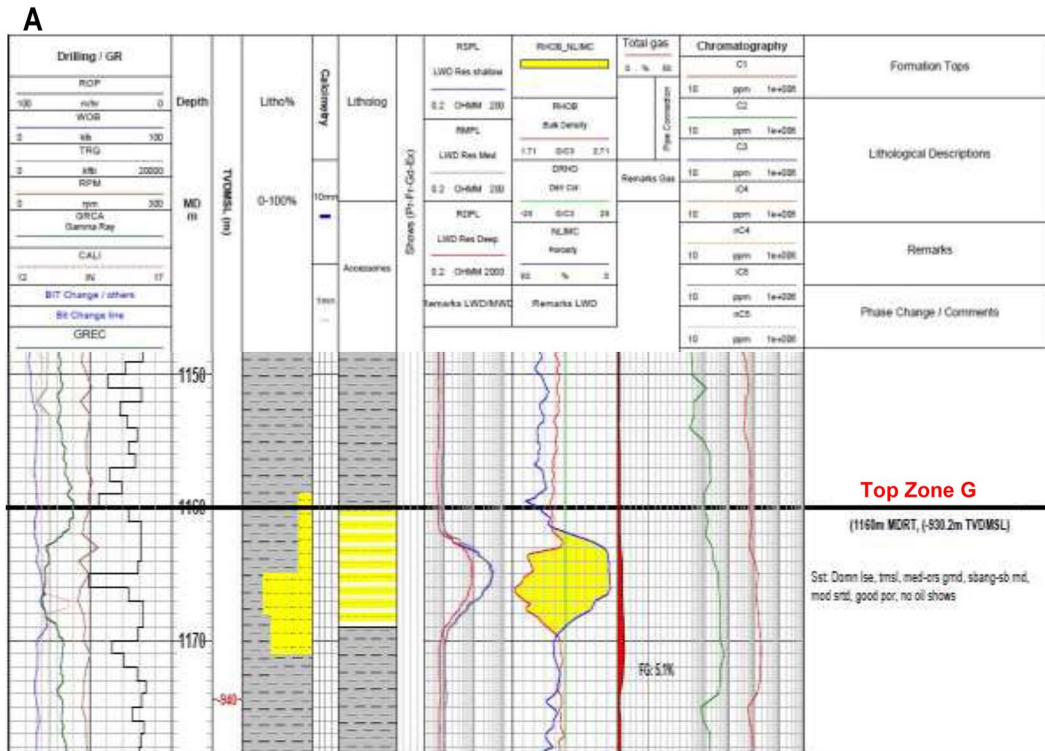
Fig. 12 A Composite log shows the high values of the chromatograph analysis and the high deep resistivity values opposite zone F within Tao-5 STA Well between measured depths 3169 and 3215 m. **B**

Petrophysical data with interpretation for zone F represents the highly promising characteristics for gas production for zone F

by obvious direct hydrocarbon indicators (flat and bright spots) on the seismic profiles which enhanced the industrial success rate to reach approximately 90% (Samuel et al. 2003; Dolson et al. 2005). In North Sinai Concession, several bright spots within the Pliocene–Quaternary section overlies

the Messinian evaporites were already drilled with proven gas discoveries (Ewida and Darwesh 2010). Figures 4 and 5 show several bright spots for the thick gas-bearing sandy intervals close to the drilled wells, but the examined zones in the present work don't display these bright spots, because

Fig. 13 A Composite log shows the high values of the chromatograph analysis and the high deep resistivity values opposite zone G within Tao-7 Well between measured depths 1162 and 1169 m. **B** Petrophys-ical data with interpretation for zone G represents the highly promis-ing characteristics for gas production for zone G

they are sub-seismic resolution according to its relatively small thickness.

The Pliocene targets in the study area are primarily expected to host primarily biogenic gas sourced from the Pliocene shale (of Kafr El-Sheikh Formation) above and beneath the sandstone reservoirs (Vandré et al. 2007; Leila and Moscariello 2017). Moreover, the abundance of listric

faults in North Sinai Concession played an essential role in forming these targets. The northward progradation of the post-Messinian sediments over the mobile Messinian evapo-rites created a series of these listric faults which detach-ing at the Messinian salt. The movements on these faults created a group of rollover folds which forming the main structural traps in the study area and surroundings (Ewida
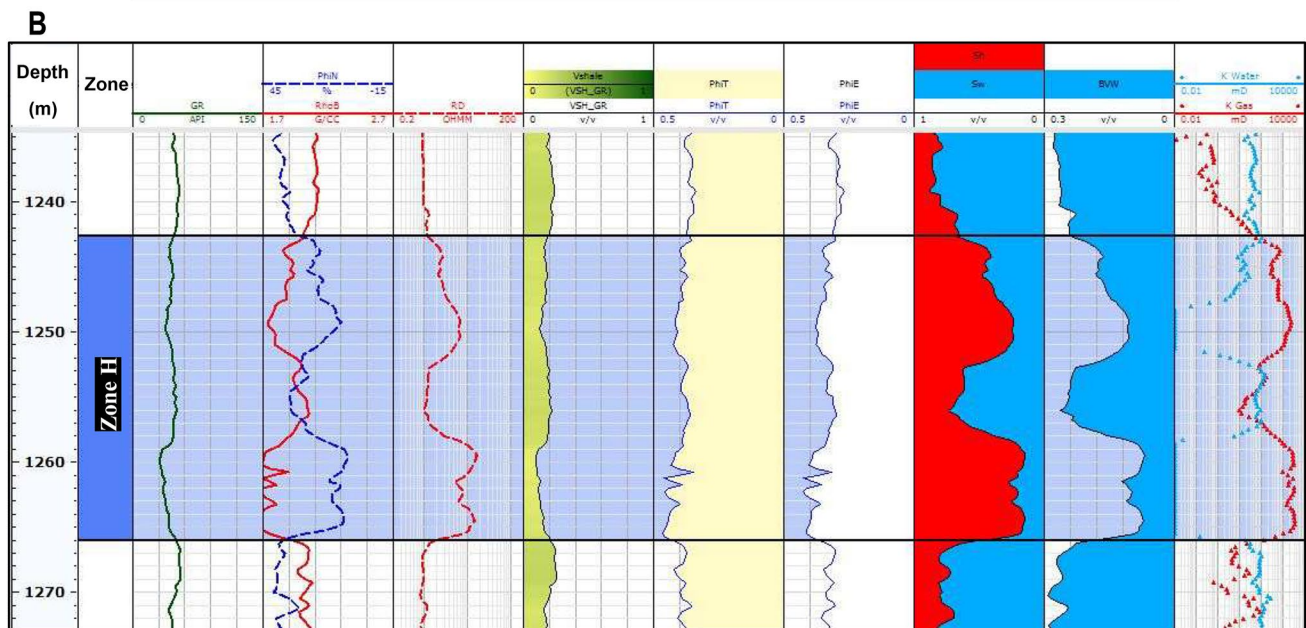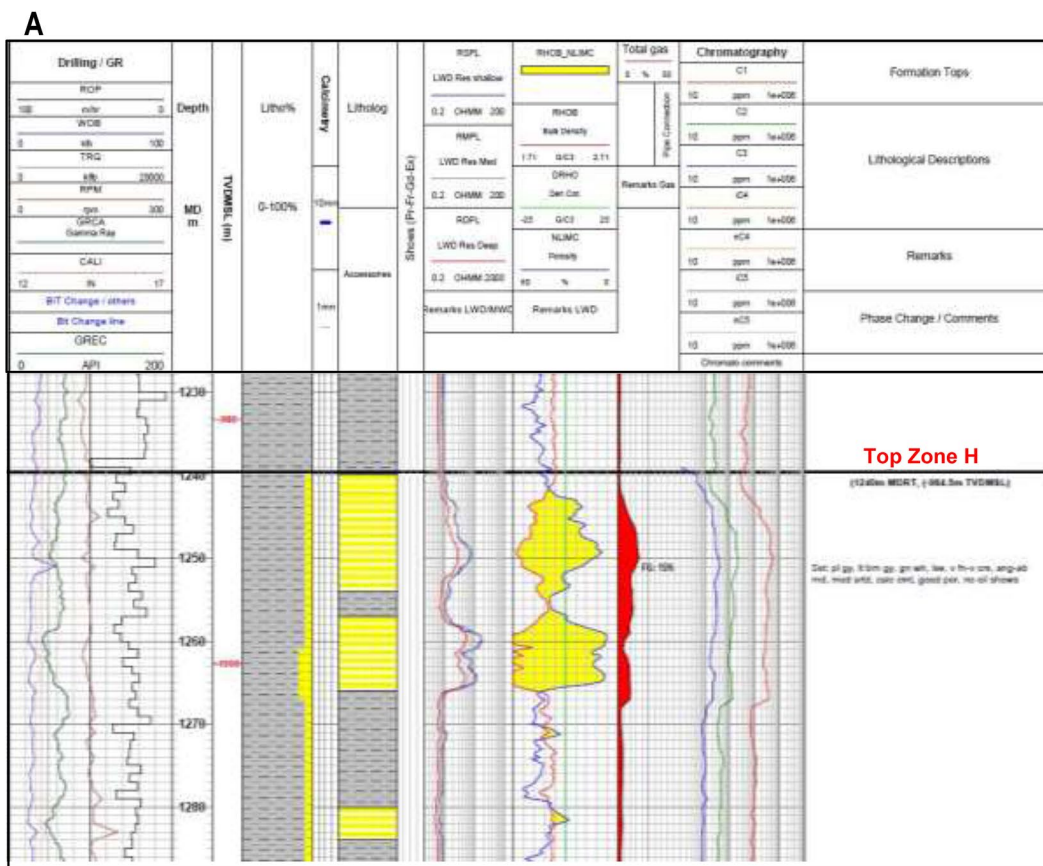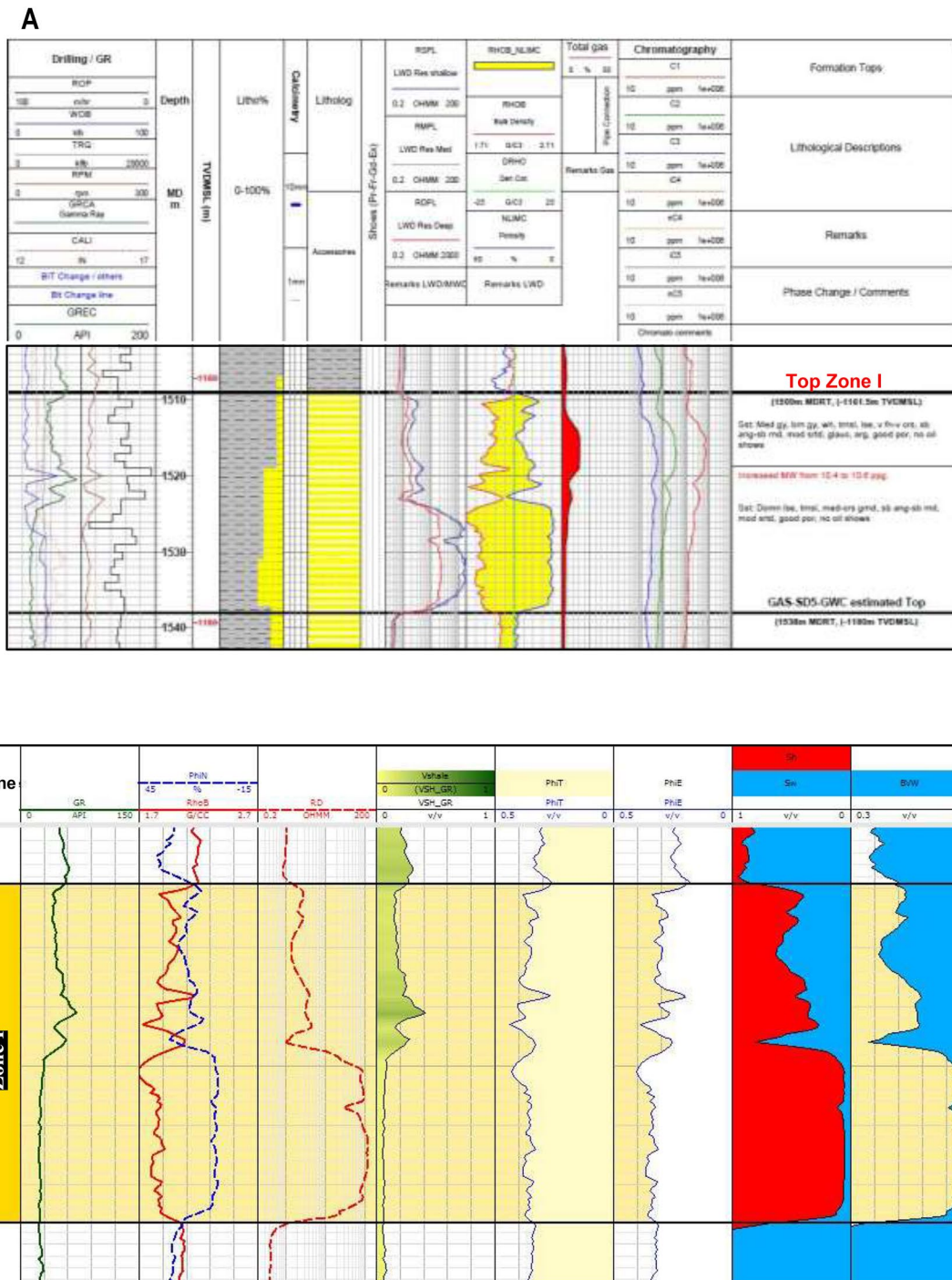
Fig. 14 **A** Composite log shows the high values of the chromatograph analysis and the high deep resistivity values opposite zone H within Tao-7 Well between measured depths 1242 and 1266 m. **B** Petrophys-ical data with interpretation for zone H represents the highly promising characteristics for gas production for zone H

Fig. 15 A Composite log shows the high values of the chromatograph analysis and the high deep resistivity values opposite zone I within Tao-7 Well between measured depths 1509 and 1538 m. B Petrophys- ical data with interpretation for zone I represents the highly promis- ing characteristics for gas production for zone I

and Darwesh 2010). Figures 4 and 5 display clear examples of these listric faults and the related rollover folds. The upthrown fault blocks represent large structural closures and therefore they form significant exploration targets (Abdel Aal et al. 2000).

Throughout the Pliocene, the offshore portion of Nile Delta Basin was characterized by N–S linear turbidite channels. These channels extend over 120 km and are variable in width up to 5 km (Fig. 21). During the late Early Pliocene times (Late Zanclean ~ 3.8 Ma), forced regression
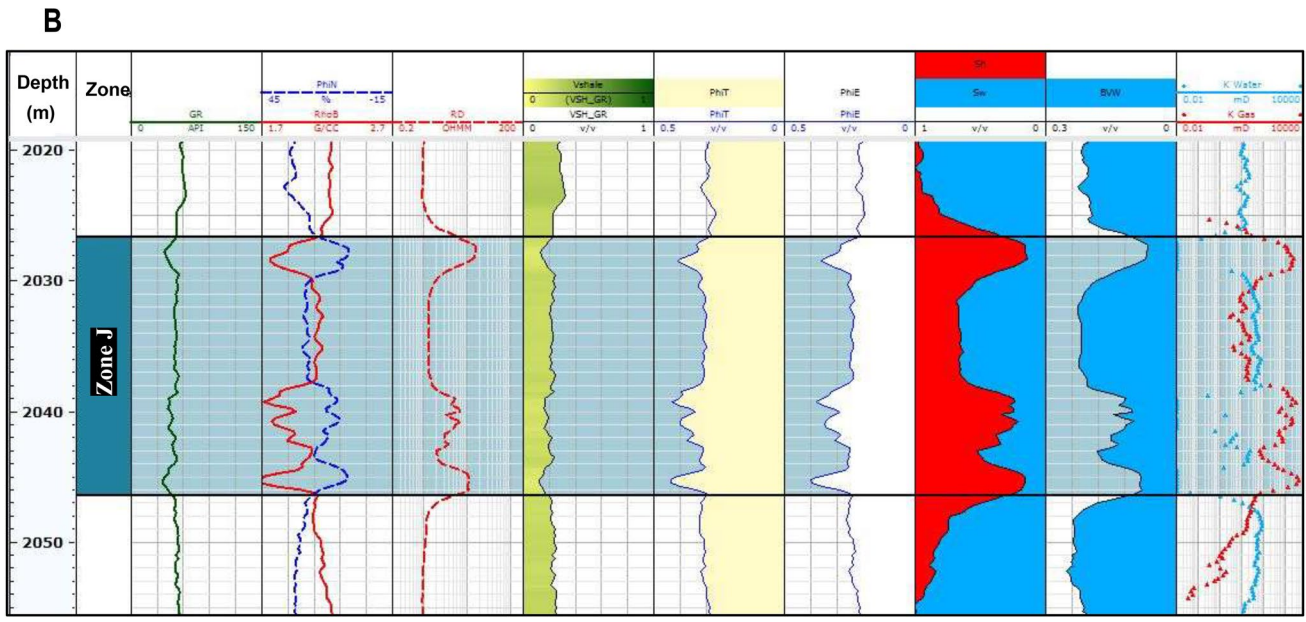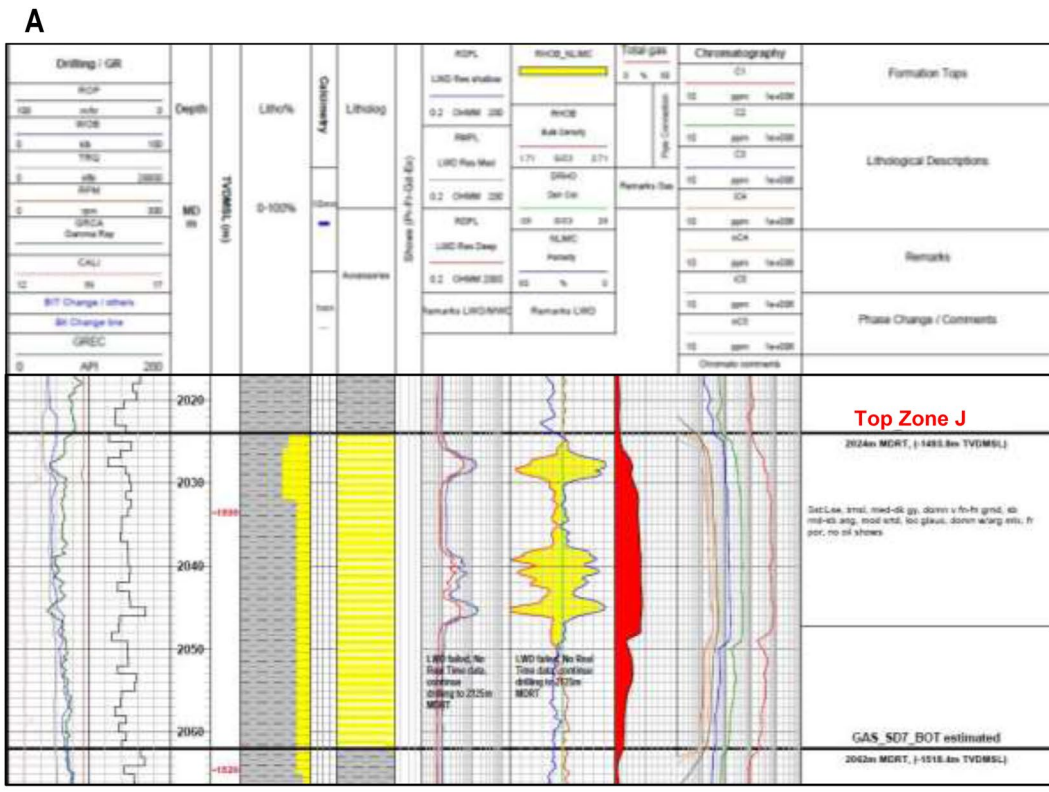
Fig. 16 A Composite log shows the high values of the chromatograph analysis and the high deep resistivity values opposite zone J within Tao-7 Well between measured depths 2027 and 2046 m. **B** Petrophysical data with interpretation for zone J represents the highly promising characteristics for gas production for zone J

phase in the Mediterranean Sea level was prevailed which resulted in the development of several progradational sequences (Dolson et al. 2005). The retreat of the Mediterranean shoreline led to the accumulation of coastal and fluvial deposits in the Nile Delta Basin (e.g. Loncke et al. 2002; Zachos et al. 2001). Throughout this phase, the deltaic sedimentation process prevailed in deep-water part as turbidities with well-developed slope channels and distal
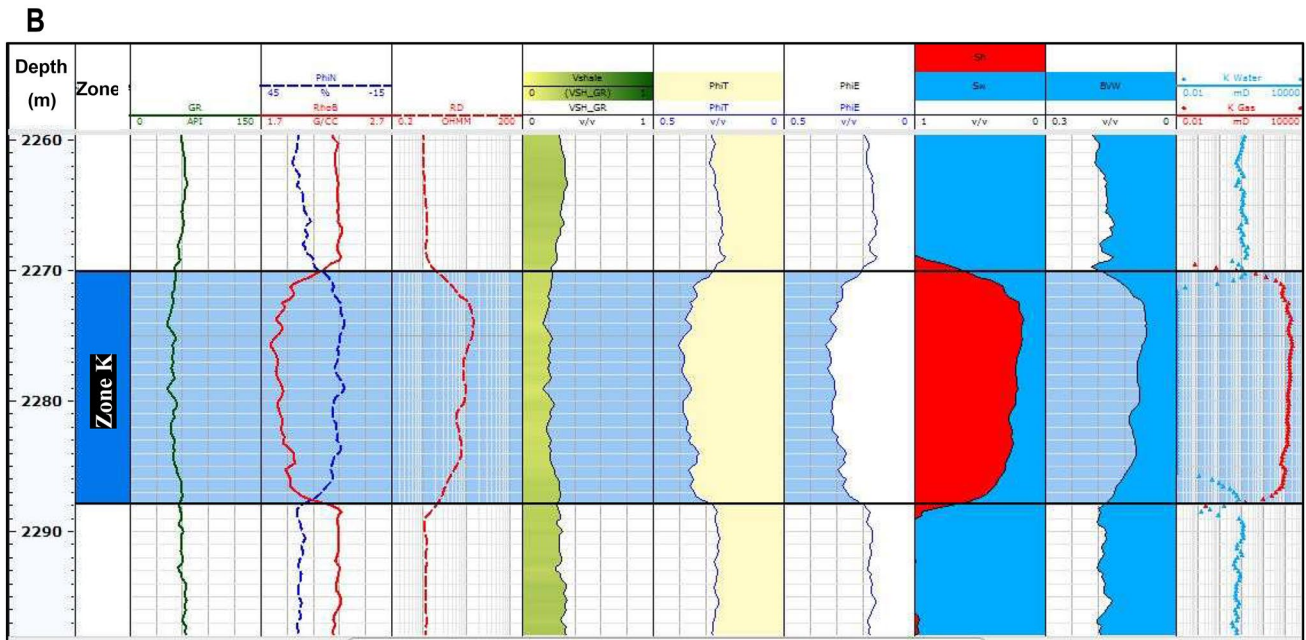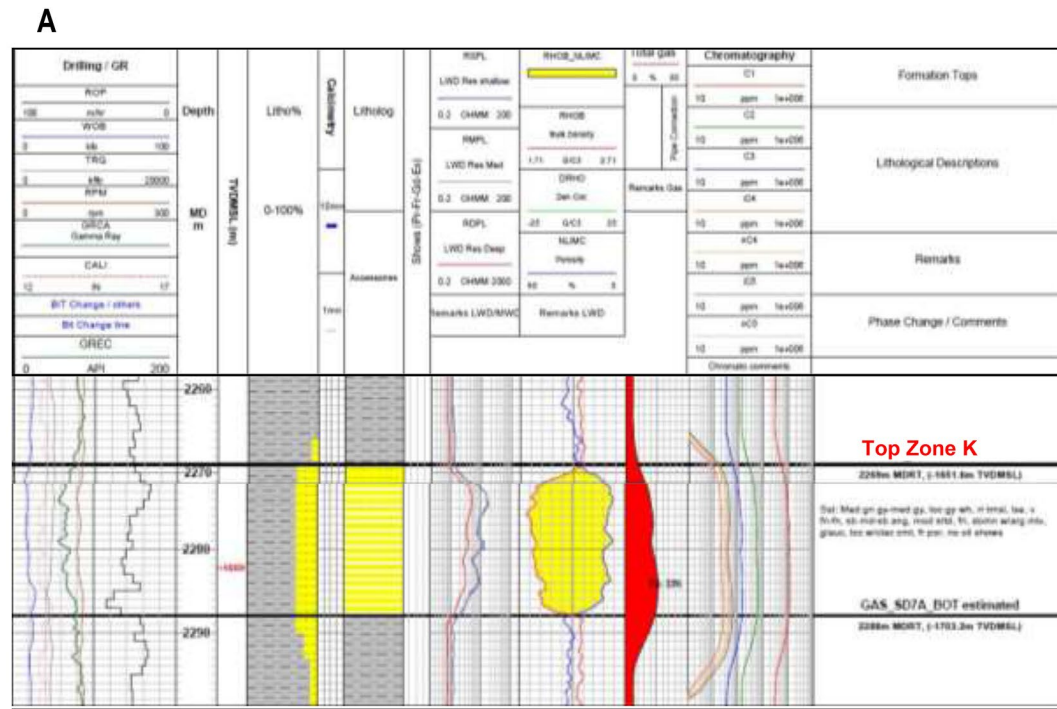
Fig. 17 A Composite log shows the high values of the chromatograph analysis and the high deep resistivity values opposite zone K within Tao-7 Well between measured depths 2270 and 2288 m. **B** Petrophys-ical data with interpretation for zone K represents the highly promising characteristics for gas production for zone K

fans (Dolson et al. 2005; Leila and Mohamed 2020). The shape of the Nile Delta is asymmetric as it is characterized by steep eastern side due to very rapid sedimentation of the Plio–Pleistocene sediments. However, the western side is gentler and more dominated by extensive slope channel

systems (Dolson et al. 2005; Leila and Mohamed 2020) as displayed in Fig. 21.

The gas-bearing zones in the present work represent sheet sands inside Kafr El-Sheikh Formation. These sands were bypassed through confined flow (updip channels) and were

Fig. 18 Pickett plots for zones A, B and C in Tao-3 ST1 Well. Note that the plotted points which are located below line $Sw = 50\%$ reflect the gas pay for each zone. Note: Points outlined by dotted-blue polygon which clustered below line $Sw = 50\%$ represent the most promising points for being gas reservoirs
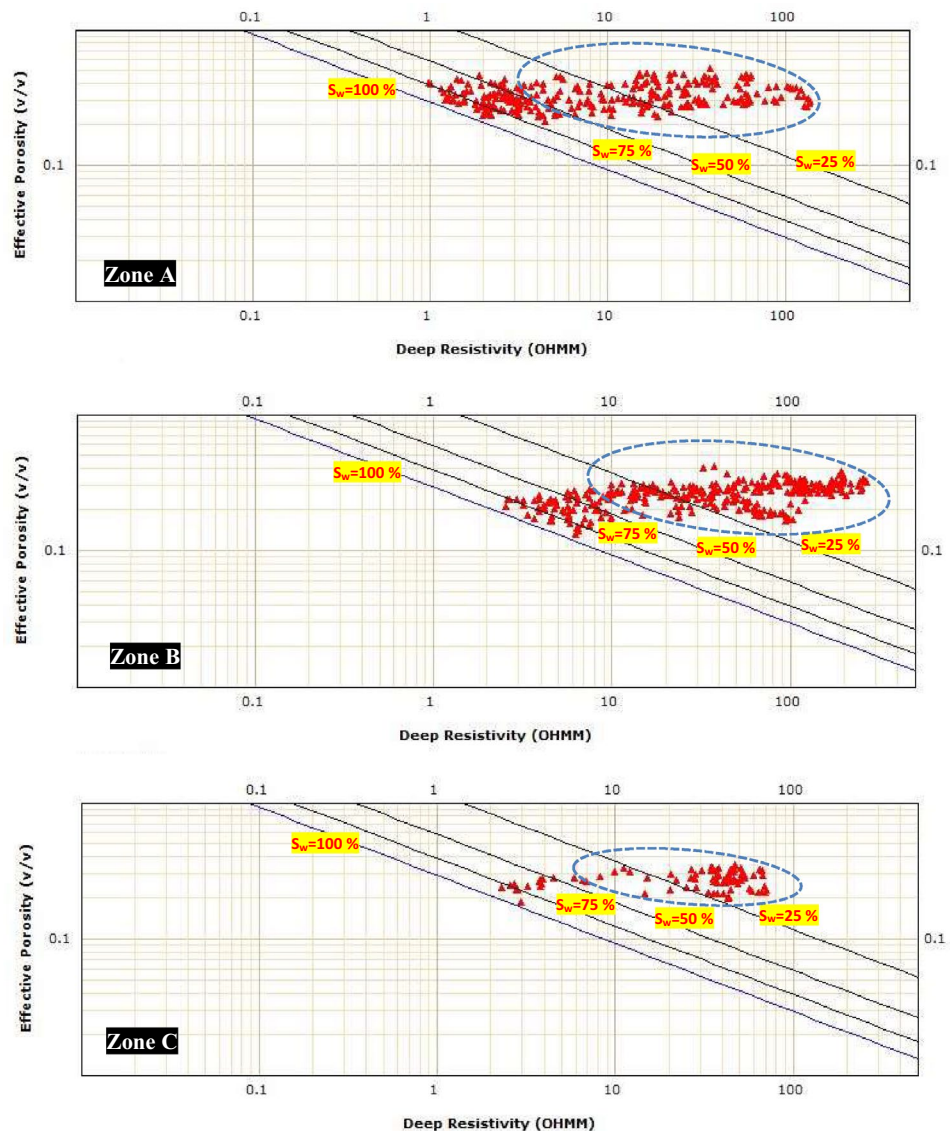
deposited in an unconfined downdip setting due to the slowing down of flows at the ends of channels. Commonly, the extension of sheet sands exceeds the area of the trap (Slatt 2006). Sheet sand is considered one of the best reservoirs in deep water, because it represents the simplest reservoir geometry and has good vertical and lateral continuity, high width/thickness ratio (more than 500:1) and small range in grain size (Chapin et al. 1994; Mahaffie 1994).

Although 88 TCF of natural gas reserve has already been discovered in Nile Delta Basin including the new significant discoveries, such as Zohr Field (Ismail et al. 2020), the Geology of the Nile Delta is still lacking detailed investigation due to the limited subsurface data and additional exploration activities are required in the future (Ismail et al. 2020). Also, the identification of the deep-water reservoirs is difficult and signifies a challenge due to the complexity of depositional system and the limited exploration level (Reilly 2016).

Moreover, studying the reservoir facies and diagenetic pathways is vital for expecting the distribution of different diagenetic characteristics which strongly control the quality and reduce the exploration risks for these shallow Pliocene gas reservoirs in the Nile Delta (Leila and Mohamed 2020).

Conclusions

The Post-Messinian megasequence of Nile Delta Basin is a wealth of natural gas reserves. The Pliocene–Pleistocene sequence in TAO Field, North Sinai Concession, offshore Nile Delta Basin has a great potentiality for holding gas reservoirs at shallow depths. The analysis of well logging data for three deviated wells (Tao-3 ST1, Tao-5 STA and Tao-7), revealed that eleven sand-intervals located within Kafr El-Sheikh Formation are gas-holding zones. These zones vary
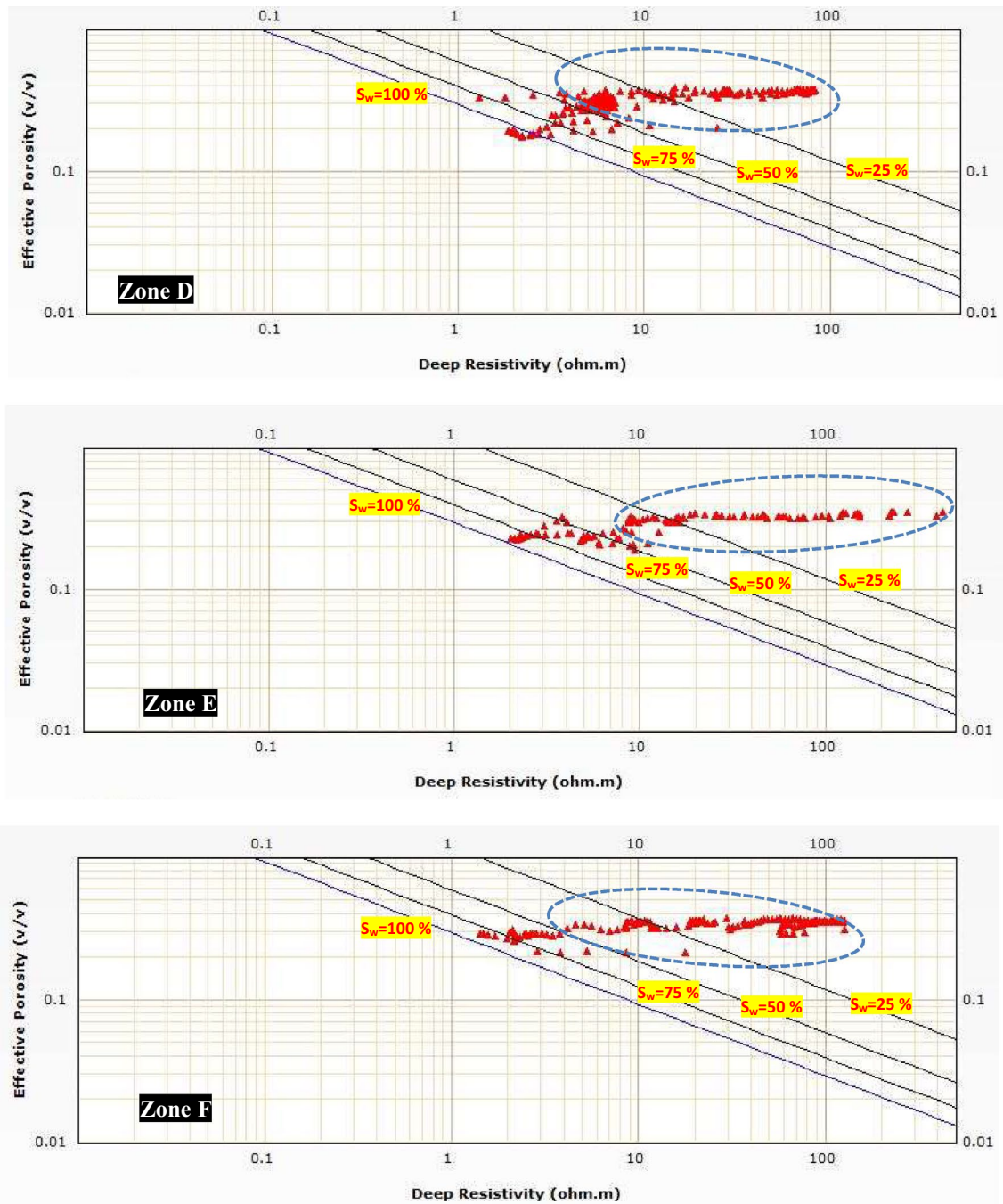
Springer
مدينة الملك عبدالعزيز
KACST للعلوم والتقنية

Fig. 19 Pickett plots for zones D, E and F in Tao-5 STA Well. Note that the plotted points which are located below line $Sw=50\%$ reflect the gas pay for each zone. Points outlined by dotted-blue polygon which clustered below line $Sw=50\%$ represent the most promising points for being gas reservoirs

in thickness from 4 up to 56 m. The calculated petrophysical parameters for these intervals display highly promising characteristics for gas production, including low shale volume (around 10%), high total porosity (30–40%), high effective porosity (30–35%), low water saturation (10–50%), low bulk volume water, increase in values of effective gas permeability and the decrease in water permeability.

The thick gas plays within the post-Messinian megasequence in North Sinai Concession exhibit noticeable direct hydrocarbon indicators (bright spots) on the seismic data which enhanced the industrial success rate. Moreover, the listric faults and the related rollover folds played significant role in forming structural traps for the gas-bearing zones in Tao Field and its surroundings. Consequently,
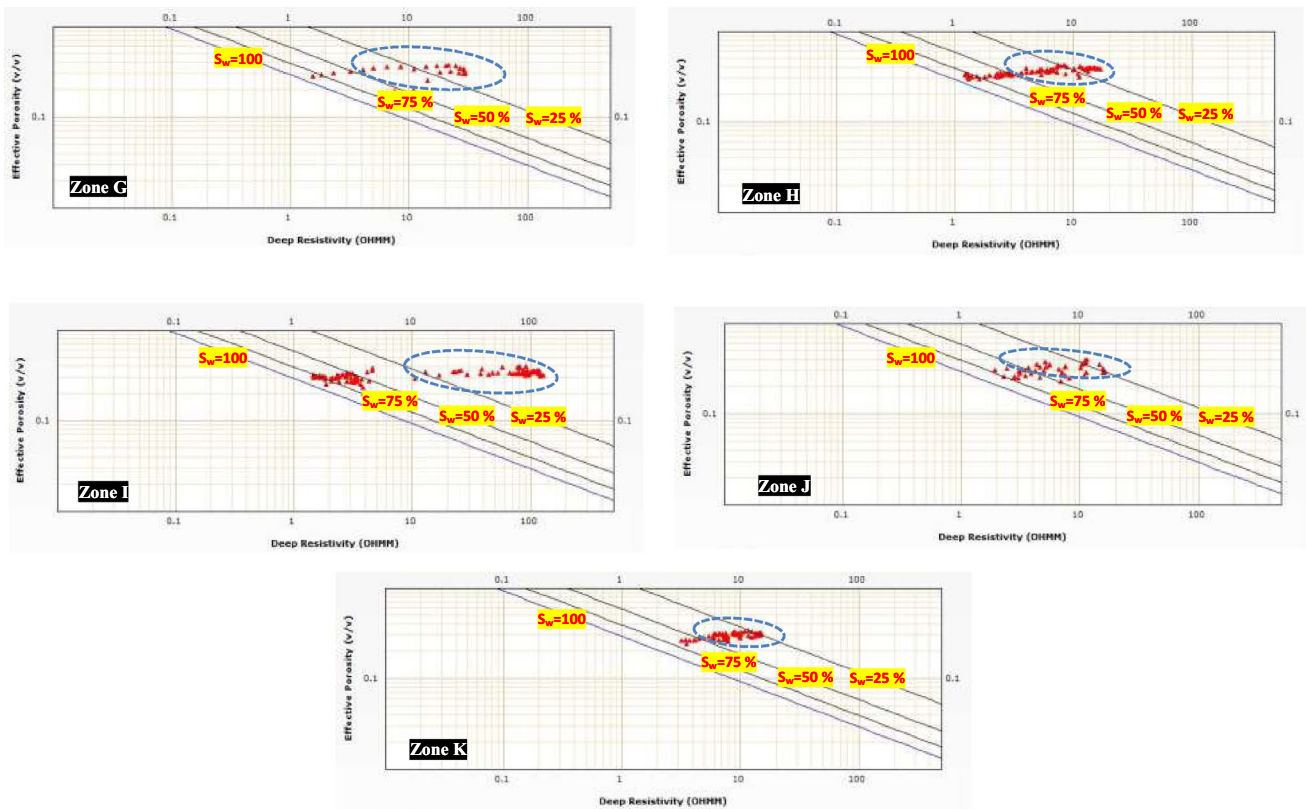
Fig. 20 Pickett plots for zones G, H, I, J and K in Tao-7 Well. Note that the plotted points which are located below line $Sw = 50\%$ reflect the gas pay for each zone. Points outlined by dotted-blue polygon which clustered below line $Sw = 50\%$ represent the most promising points for being gas reservoirs
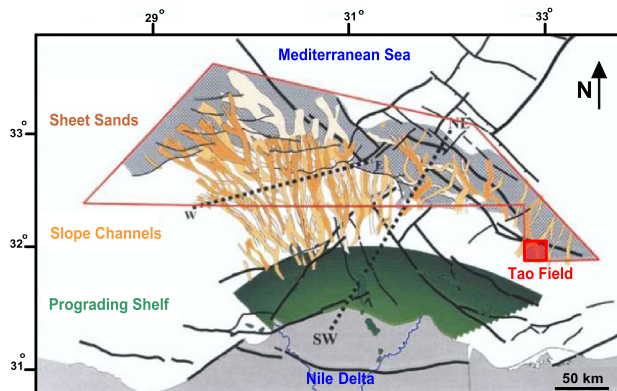

Fig. 21 Map represents the location of the Tao Field and the Pliocene depositional system in the offshore parts of Nile Delta Basin (After, Abdel Aal et al. 2000)

it is highly recommended for the North Sinai Petroleum Company (the honour of the examined concession) to drill new wells cut through every bright spot in the study area for discovering additional possible gas-bearing reservoirs.

Declarations

Conflict of interest Here, I confirm that there is no conflict of interest.

Ethical statements Hereby, I assure that this paper has not been previously published and the manuscript reflects my own research and analysis in a truthful and complete manner.

References

Abd-Allah A (2008) Mesozoic-Cenozoic inversion tectonics of North Sinai: integration of structural and basin analysis. J Appl Geophys 7:77–108

Abd-Allah AM, Abd El-Naby A, Aal MHA (2020) Tectonic and basin evolution of South Eastern Mediterranean for hydrocarbon potentiality in North Sinai, Egypt. J Pet Sci Eng 190:107080

Abdel Aziz H, Shann M (2005) Egypt: gas discoveries since 2000–continued, consistent success. Lead Edge 24(3):242–244

Abdel Aal A, El Barkooky A, Gerrits M, Meyer H, Schwander M, Zaki H (2000) Tectonic evolution of the Eastern Mediterranean Basin and its significance for hydrocarbon prospectively in the ultra-deep water of the Nile Delta. Lead Edge 19(10):1086–1102

Abd El-Gawad EA, Abdelwahhab MA, Bekiet MH, Noah AZ, ElSayed NA, Abd Elhamed EF (2019) Static reservoir modeling of El Wastani formation, for justifying development plans, using 2D seismic and well log data in Scarab field, offshore Nile Delta, Egypt. J Afr Earth Sci 158:103546

Asquith G, Gibson C (1982) Basic well log analysis for geologists: methods in exploration series. AAPG, Tulsa, Oklahoma.

Barber PM (1981) Messinian subaerial erosion of the Proto-Nile Delta. Mar Geol 44:253–272

Buckles RS (1965) Correlating and averaging connate water saturation data. J Can Pet Technol 4(1):42–52

Chapin MA, Davies P, Gibson JL, Pettingill HS (1994) Reservoir architecture of turbidite sheet sandstones in laterally extensive outcrops, ross formation, Western Ireland. In: Weimer P, Bouma AH, Perkins BF (Eds.), Submarine fans and turbidite systems, GCS–SEPM foundation 15th annual Research Conference, pp. 53–68.

Dolson JC, Boucher PJ, Dodd T, Ismail J (2002) The petroleum potential of the emerging Mediterranean offshore gas plays Egypt. Oil Gas J 100(20):32–37

Dolson JC, Boucher PJ, Siok J, Heppard P (2005) Key challenges to realizing full potential in an emerging giant gas province: Nile Delta/Mediterranean offshore, deep water, Egypt. In: Doré AG, Vining BA (eds) Petroleum geology: North–West Europe and global perspectives, geological society, London, petroleum geology conference series no. 6, proceedings on 6th petroleum geology conference, pp 607–624

Dolson JC, Shann MV, Matbouly S, Harwood C, Rashed R, Hammouda H (2001) The petroleum potential of Egypt. In: Downey MW, Threet JC, Morgan WA (eds) Petroleum provinces of the Twenty-first century. AAPG Memoir 74, Tulsa

Egyptian General Petroleum (EGPC) (1994) Nile Delta and North Sinai: fields, discoveries and hydrocarbon potential (a comprehensive overview). Egypt, Cairo

Elatrash AM, Abdelwahhab MA, Wanas HA, El-Naggar SI, Elshayeb HM (2021) Well log-aided source rock potential, basin modeling, and seismic attributes: petroleum geology case study of Pliocene discovery at South Mansoura Area (Nile Delta). Arab J Geosci 14(10):1–10

El-Fawal FM, Sarhan MA, Collier REL, Basal A, Aal MHA (2016) Sequence stratigraphic evolution of the post-rift megasequence in the northern part of the Nile Delta Basin. Egypt Arabian Journal of Geosciences 9(11):585

Esestime P, Hewitt A, Hodgson N (2016) Zohr–a newborn carbonate play in the Levantine Basin East-Mediterranean. First Break. https://doi.org/10.3997/1365-2397.34.2.83912

Ewida HF, Darwesh MS (2010) Hydrocarbon plays and prospectivity from possible seismic hydrocarbon indicators in offshore North Sinai. MOC, Alexandria, Egypt.

Fertl W, Frost E (1980) Evaluation of shaly clastic reservoir rocks. J Pet Technol 32(9):1641–1645

Gardner GHF, Gardner LW, Gregory AR (1974) Formation velocity and density; the diagnostic basics for stratigraphic traps. Geophysics 39(6):770–780

Hammond AL (1974) Bright spot: better seismological indicators of gas and oil. Science 185(4150):515–517

Haq BU, Hadenbol J, Vail PR (1987) Chronology of fluctuating sea levels since the Triassic. Science 235(4793):1156–1167. https://doi.org/10.1126/SCIENCE.235.4793.1156

Harms JC, Wray JL, (1990) Nile Delta. In Said R (Ed) Geology of Egypt, AlBalkema, Rotterdam, Netherlands, pp 329–343.

Ismail A, Ewida HF, Al-Ibiary MG, Zollo A (2020) Integrated prediction of deep-water gas channels using seismic coloured inversion and spectral decomposition attribute, West offshore, Nile Delta Egypt. NRIAG J Astron Geophys 9(1):459–470

Kirschbaum MA, Schenk CJ, Charpentier RR, Klett TR, Brownfield ME, Pitman JK, Cook TA, and Tennyson ME (2010) Assessment of undiscovered oil and gas resources of the Nile Delta Basin Province, Eastern Mediterranean (no. 2010–3027). US Geological Survey.

Lashin A, Mogren S (2012) Analysis of well log and pressure data of the gas-bearing sand reservoirs of Kafr El-Sheikh formation: case study from the off-shore Nile Delta-Egypt. Int J Phys Sci 7(35):5353–5366

Leila M, Mohamed A (2020) Diagenesis and petrophysical characteristics of the shallow Pliocene sandstone reservoirs in the Shinfas Gas Field, onshore Nile Delta Egypt. J Pet Explor Prod Technol 10(5):1743–1761

Leila M, Moscariello A (2017) Organic geochemistry of oil and natural gas in the West Dikirnis and El-Tamad fields onshore Nile Delta, Egypt: interpretation of potential source rocks. J Petrol Geol 40:37–58

Loncke L, Gaullier V, Bellaiche G, Mascle J (2002) Recent depositional patterns of the Nile deep-sea fan from echo-character mapping. AAPG Bull 86:1165–1186

Lourens LJ, Antonarakou A, Hilgen FJ, Van Hoof AAM, Vergnaud-Grazzini C, Zachariasse WJ (1996) Evaluation of the Plio-Pleistocene astronomical timescale. Paleoceanography 11(4):391–413

Loutit TD, Allard JC, Dolson J, and Schruers Laura S (2001) A new view of Egypt's hydrocarbon potential (abs.): Middle East and North Africa (MENA).

Mahaffie, M.J., (1994). Reservoir classification for turbidite intervals at the Mars discovery, Mississippi Canyon 807, Gulf of Mexico. In: Weimer P, Bouma AH, Perkins BF (Eds.), Submarine fans and turbidite systems, GCS–SEPM Foundation 15th annual research conference, pp 233–244.

May PR (1991) The Eastern Mediterranean Mesozoic Basin: evolution and oil habitat. AAPG Bull 75:1215–1232

Mohamed, AAEH (2004) Reservoir characterization and depositional patterns of pliocene and miocene in the North Nile Delta, Mediterranean Sea, Egypt. In American Association of Petroleum Geologist (AAPG) international conference, October pp 24–27, 2004; Cancun, Mexico.

Moustafa AR, Khalil MH (1995) Superposed deformation in the northern Suez Rift, Egypt: relevance to hydrocarbons exploration. J Pet Geol 18(3):245–266

Othman AA, Fathy M, Negm A (2018) Identification of channel geometries applying seismic attributes and spectral

decomposition techniques, Temsah field, Offshore East Nile Delta Egypt. NRIAG J Astron Geophys 7(1):52–61

Pickett, G., R. (1972). Practical formation evaluation. Golden, Colorado, G.R. Pickett, Inc.

Poupon A, Leveaux J (1971) Evaluation of water saturation in shaly formations. In SPWLA 12th annual logging symposium. Society of Petrophysicists and Well-Log Analysts.

Reilly JM (2016) Marine broadband technology: history and remaining challenges from an end-user perspective. Lead Edge 35(4):316–321. https://doi.org/10.1190/tle35040316.1

Ruggieri G, Sprovieri R (1976) Messinian salinity crisis and its paleogeographical implications. Palaeogeogr Palaeoclimatol Palaeoecol 20(1–2):13–21

Salem AM, Ketzer JM, Morad S, Rizk RR, Al-Aasm IS (2005) Diagenesis and reservoir-quality evolution of incised valley sandstones: evidence from the Abu Madi gas reservoirs (Upper Miocene), the Nile Delta Basin, Egypt. J Sed Res 75:572–584

Samuel A, Kneller B, Raslan S, Sharp A, Parsons C (2003) Prolific deep-marine slope channels of the Nile Delta. Egypt AAPG Bull 87:541–560

Sarhan MA, Safa MG (2019) 2D seismic interpretation and hydrocarbon prospects for the neogene-quaternary succession in the Temsah field, offshore Nile Delta Basin Egypt. J Afr Earth Sci 155:1–12

Sarhan MA, Collier REL, Basal AMK, Abdel Aal MH (2014) Late Miocene normal faulting beneath the Northern Nile Delta: NNW propagation of the Gulf of Suez Rift. Arab J Geosci 7(11):4563–4571

Sestini G (1989) Nile Delta: a review of depositional environments and geological history. Geol Soc London Special Publ 41(1):99–127

Slatt RM (2006) Stratigraphic reservoir characterization for petroleum geologists, geophysicists, and engineers. Elsevier, Amsterdam, p 478

Vandré C, Cramer B, Gerling P, Winsemann J (2007) Natural gas formation in the western Nile Delta (Eastern Mediterranean): thermogenic versus microbial. Org Geochem 38(4):523–539

Zachos J, Pagani M, Sloan L, Thomas E, Billups K (2001) Trends, rhythms, and aberrations in global climate 65 Ma to present. Science 292:686–693